Article:
Abdpour, S, Kowsari, E, Bazri, B et al. (8 more authors) (2020) Amino-functionalized MIL-101(Cr) photodegradation enhancement by sulfur-enriched copper sulfide nanoparticles: An experimental and DFT study. Journal of Molecular Liquids, 319. 114341. p. 114341. ISSN 0167-7322

https://doi.org/10.1016/j.molliq.2020.114341

Amino-functionalized MIL-101(Cr) photodegradation enhancement by Sulfur-enriched copper sulfide nanoparticles: An experimental and DFT study

Soheil Abdpour[a], Elaheh Kowsari[a], Behrouz Bazri[a], Mohammad Reza Alavi Moghaddam[b], Saeedeh Sarabadani Tafreshi[a], Nora H. de Leeuw[c,d], Ilka Simon[e], Laura Schmolke[e], Dennis Dietrich[e], Seeram Ramakrishna[f], Christoph Janiak[e]*

[a] Department of Chemistry, Amirkabir University of Technology, No. 424, Hafez Avenue, 1591634311 Tehran, Iran

[b] Department of Civil &Environmental Engineering, Amirkabir University of Technology, Hafez Avenue, Tehran 15875-4413, Tehran, Iran

[c] School of Chemistry, Cardiff University, Main Building, Park Place, Cardiff CF10 3AT, United Kingdom

[d] now at: School of Chemistry, University of Leeds, Leeds LS2 9JT, United Kingdom

[e] Institut fur Anorganische Chemie und Strukturchemie, Universität Düsseldorf, 40204 Düsseldorf, Germany

[f] National University of Singapore, Nanoscience and Nanotechnology Initiative, 9 Engineering Drive 1, Singapore, 117576, Singapore

Abstract

In the present work, a direct Z-scheme composite photocatalyst, NH_2-MIL-101(Cr)@CuS, with high photodegradation efficiency of Rhodamine B (RhB) degradation in the visible light spectrum, is fabricated through a solvothermal method. It was found that the NH_2-MIL-101(Cr)@CuS composite with an appropriate amount of NH_2-MIL-101(Cr) exhibited high catalytic performance in the RhB photodegradation. The photocurrent density and results from the electrochemical impedance spectroscopy (EIS) analysis confirm the promoted photocatalytic activity of the NH_2-MIL-101(Cr)@CuS composite compared to the pristine MIL-101(Cr) and CuS nanoparticles, which were supported by the electron lifetime (τ_n) calculations for the samples. The trapping experiments and Mott-Schottky analysis revealed that the superoxide radicals ($^{\bullet}O_2^-$) played an essential role in the photodegradation of RhB and the promoted photocatalytic activity contributed to a direct Z-scheme mechanism between CuS and NH_2-MIL-101(Cr). Stability study also shows acceptable results during photocatalytic reaction. Furthermore, Density Functional Theory (DFT) calculations were performed to gain a better understanding of the electronic properties of the NH_2-MIL-101(Cr)@CuS nanocomposite. The calculated band structures showed that the nanocomposite has a higher photocatalytic efficiency in the visible region compared to the pristine MIL-101(Cr) and CuS. The calculated band gap of both the semiconductors and the hybrid nanocomposite confirms the experimental results.

Keywords: Metal-Organic Frameworks, Copper Sulfide Nanoparticles, Photocatalyst, Rhodamine B, Direct Z-scheme mechanism, density functional theory calculations

1- Introduction

The increase in urban and industrial activities of our societies has led to growing amounts of pollutants being released into the environment, which causes severe problems for water quality. The presence of organic dyes in water resources, used for example, in industrial processes for textiles, food, leather, paint or coatings, leads to many problems such as non-aesthetic, eutrophication, and they also endanger human health[1,2]. There are several traditional techniques for the remediation of dye molecules in wastewater, including physical and biological technologies that are, however, incapable of achieving efficient degradation of the dye molecules[3–8]. In recent years, interest has grown into the use of solar energy and semiconductor photocatalysis in water purification, e.g., the pollutants degradation process, the photocatalytic green fuel production, and the conversion of greenhouse molecules into fuels or chemicals[9–12]. Also, the specific functionalization of compounds for specific roles in their environment and targeting using green surfactants has a bright future[13,14]. Several photocatalytic materials, including metal oxides, metal sulfides, metal phosphides, and metal-organic frameworks (MOFs), have been studied for water purification through the photodegradation of pollutants molecules[15–19]. Some innovative findings include in the study on the composite products with enhanced morphology as well as the improved Z-scheme- charge-carriers separation and plasmon-induced injection for the photocatalytic process[20,21], increasing the utilization efficiency of visible light by doping [22], and the new combination of the process like the interaction between photocatalysts and microorganisms[23].

Copper (II) sulfide (CuS) is one of the most promising semiconductor materials with excellent optical, electronic, chemical, and thermal properties[24–31]. It is a p-type semiconductor with a broad reported range for its bandgap (1.63- 2.56 eV)[32,33]. CuS has attracted much attention as

64 a co-catalyst to improve the photocatalytic performance of a wide range of materials, e.g., in
65 combination with metal oxides and metal sulfides, as well as carbonaceous graphitic carbon nitride
66 (g-CN), and also for the fabrication of efficient hybrid/composite materials with carbon-based
67 materials like graphene oxide for energy conversion applications[34–37].

68 Metal-organic frameworks define as hybrid inorganic/organic crystalline materials designed as
69 metal clusters and organic linkers, which have the potential application of impurity removal in
70 aqueous solutions[38–41]. Flexibility in the linker design of MOFs, their high surface area and
71 porosity have led to the use of MOFs in various scientific and technological fields, including gas
72 storage, gas separation, drug delivery, sensors, supercapacitors, heat transfer, water adsorption,
73 catalytic and photocatalytic applications[8,42–44]. Alvaro et al.[45] first proposed MOF-5 as a
74 catalyst for the photodegradation of water contaminants, and after that, many types of research
75 studies have focused on MOFs as photoactive materials for energy applications[45–48]. However,
76 pure MOFs have drawbacks as photocatalysts, corresponding to a high electron-hole
77 recombination rate and partial adsorption of UV-visible irradiation[49–51]. Different groups of
78 materials, including conventional semiconductor materials (TiO_2, ZnO, CdS, ZnS), carbon-based
79 materials (graphene oxide, g-CN), and even diverse types of MOFs have been used to fabricate
80 active hybrid/composite photocatalysts with enhanced photocatalytic performance compared to
81 pure MOFs and other parent materials[52–55]. Among these diverse strategies for developing
82 efficient hybrid/composite photocatalysts, semiconductor@MOF photocatalysts have shown
83 considerable advantages, resulting from the synergistic effect between MOFs and conventional
84 semiconductors[56]. Many semiconductor nanoparticles have been used for developing
85 semiconductor@MOF systems to date, including CdS@MIL-101(Cr), ZnO@ZIF-8, TiO_2@UiO-
86 66, ZnO@MOF-5, CdS@MIL-53(Fe), CdS@MIL-100(Fe), and Bi_2S_3@MIL-100(Fe)[56–60].

Recently, the main focus of researchers for developing new semiconductor@MOF photocatalysts is to identify new combinations of MOFs and semiconductor materials that use a direct Z-scheme charge separation mechanism, which, compared to traditional type-II band-to-band charge separation, shows higher redox capacity and more efficient charge carrier separation[61,62].

The primary purpose of this study was to explore the use of copper sulfide nanoparticles to enhance the photocatalytic efficiency of MOFs. The novel direct Z-scheme NH_2-MIL-101(Cr)@CuS composite with different weight percentages of copper sulfide was developed for the operative photodegradation of RhB in the visible light irradiation. The high surface area amino-functionalized MIL-101(Cr) with water-stable structure was used as a matrix to disperse the nanoparticles of copper sulfide, reduce their agglomeration, and also reduce the electron-hole recombination rate in the resulting composite structures compared to the parent materials[63]. In the photocatalytic degradation of RhB, electrochemical and photoelectrochemical experiments showed the excellent photocatalytic activity of the composite, owing to the effective interactions with NH_2-MIL-101(Cr) and copper sulfide nanoparticles, which may introduce these nanoparticles as a cost-effective, innocuous and operative co-catalyst for the development of photocatalytic composite systems based on MOFs.

2. Material and Methods

2.1 Materials

All the chemicals (AR grade) were used without any further purification. $Cu(NO_3)_2.6H_2O$ (98%), thioacetamide (98%), $Cr(NO_3)_3 \cdot 9H_2O$ (99%) were purchased from Sigma Aldrich. Ethylene glycol (98%), NaOH (98%), and 2-Aminoterephthalic acid (99%) were purchased from Merck Company. Nafion solution (5%) was purchased from Alfa Aesar Company.

2.2 Synthesis of CuS nanoparticles

The CuS nanoparticles are synthesized via the hydrothermal approach[64]. For this purpose, about 0.1215 g (0.41 mmol) of $Cu(NO_3)_2.6H_2O$ and 0.0765 g (1 mmol) of thioacetamide (TAA) stirred for 30 min to dissolve in 10 mL of ethylene glycol at ambient temperature. The mixture was then transferred into a 20 mL Teflon-lined container within stainless-steel autoclave cover and heated at 150 °C for 24 h. After cooling in ambient air, the obtained nanoparticles were separated by centrifugation at 10000 rpm for 10 min. The precipitate was washed three times with DI water and ethanol. The powder dried in a vacuum oven at 60 °C overnight. The final weight of the obtained CuS after washing and drying was 0.0257 g (yield 34%.).

2.3 Synthesis of NH_2-MIL-101(Cr)

The NH_2-MIL-101(Cr) nanoparticles were also synthesized *via* a hydrothermal method. Typically, 3.20 g (14.7 mmol) of $Cr(NO_3)_3 \cdot 9H_2O$ and 1.44 g (8 mmol) of 2-Aminoterephthalic acid was added gradually into 60 mL of a solution of NaOH (0.33 M). The mixture was stirred at ambient temperature for 30 min and then transferred into a 100 mL Teflon-coated stainless-steel autoclave and kept at 150 °C for 12 h. Afterwards, the cooled mixture was centrifuged at 10000 rpm for 15 min to collect the precipitate. The separated powder had green color easily visible to the naked eye. The product washed sufficient times with water, DMF, and methanol, individually, and dried overnight at 100 °C. The final weight of the NH_2-MIL-101(Cr) was 2.0 g (yield: 72 %).

2.4 Synthesis of NH_2-MIL-101(Cr)@CuS composite photocatalyst

In order to synthesize the NH_2-MIL-101(Cr)@CuS composite, diverse quantities of NH_2-MIL-101(Cr) (0.05,0.1, 0.15, 0.2, and 0.25 g) were dispersed into ethylene glycol using ultrasound for

30 min. Then 0.1215 g (0.41 mmol) of $Cu(NO_3)_2 \cdot 6H_2O$ was added to the suspension and mixed for 30 min. After the complete dissolution of $Cu(NO_3)_2 \cdot 6H_2O$, 0.0756 g (1 mmol) of TAA added to the suspension and stirred for another 30 min. The resulting mixture was transferred to a Teflon-lined stainless-steel autoclave and heated at 150 °C for 24 h. The samples are called after the initial weight of NH_2-MIL-101(Cr) nanoparticles as 0.05-NM@CuS, 0.1-NM@CuS, 0.15-NM@CuS, 0.20-NM@CuS, and 0.25-NM@CuS for the products with 0.05, 0.1, 0.15, 0.2, 0.25 g of NH_2-MIL-101(Cr), respectively.

2.5 Characterization

The powder diffraction x-ray analysis (PXRD) measurement of the samples was carried out at room temperature in a BRUKER D2 Phaser in 2θ angles with Cu Kα radiation (λ = 1.54182 Å) at a voltage of 35 kV. The FT-IR spectra of the samples were recorded on a Bruker Tensor 37 IR spectrometer (Bruker Optics, Ettlingen, Germany) with the ATR unit. Scanning electron microscopy (SEM) was performed with a Jeol JSM-6510LV QSEM Advanced microscope with tungsten (Wolfram, W) cathode (5-20 keV). The Bruker Xflash 410 silicon drift detector was used in the microscope, and Bruker ESPRIT software applied for energy-dispersive X-ray spectroscopic (EDX) analysis. Transmission electron microscopy (TEM) images were taken on deposited samples on 200 µm carbon-coated gold grids using a FEI Tecnai G20, operating at an accelerating voltage of 200 kV. Selected-area electron diffraction (SAED) patterns were recorded with a FEI Tecnai G2 F20. Averaged diffraction patterns of 3 measurements were recorded and described. HR-XPS (ESCA) measurements were conducted on a Fisons/VG Scientific ESCALAB 200X xp spectrometer, functioning at 80 °C, a pressure of 1.0×10^{-9} bar, and a sampling angle of 33°. Polychromatic Al Kα excitation (11 kV, 20 mA) was used for recording spectra (emission angle: 0°, reference: carbon 1s orbital with a binding energy of 284.8 eV). A Micrometrics ASAP 2020

automatic gas sorption analyzer, armed with oil-free vacuum pumps (ultimate vacuum $<10^{-8}$ mbar), was used to measure the sorption isotherms. The samples were attached to the preparation port of the device and were degassed under high vacuum for 6 h at 120 °C. Nitrogen sorption isotherms were measured at 77 K (liquid nitrogen cooling). UV-Visible measurements were carried out with a UV-Vis SPECORD S600 (2012) from Analytik Jena, a simultaneous measuring spectrophotometer with polychromator construction and measuring the range of 190-1100 nm. The photoluminescence analysis was done by a PerkinElmer (USA) (model LS50B). The chromium leached after the photocatalytic reaction was determined by ICP-OES (730-ES, VARIAN). All electrochemical and photoelectrochemical experiments were carried out by IVIUM potentiostat/galvanostat (VERTEX entry-level instrument).

2.6 Photocatalytic tests

The photocatalytic performance of the samples was determined by photodegradation of RhB under visible light irradiation (500 W xenon lamp, with a 420 nm UV-cutoff filter) in the open air at controlled room temperature. The xenon lamp was kept at a fixed distance to the photocatalytic reactor in order to provide the standard condition (100 mW/cm^2) during photocatalytic tests. In a typical experiment, 10 mg of photocatalyst sample was dispersed into 100 mL of RhB aqueous solution (10 mg/L) in a 200 mL cylindrical Pyrex vessel reactor with a quartz window. The pH of the as-prepared suspension adjusted to 7.0. The suspension was sonicated for 15 minutes and then stirred magnetically in the dark condition for 2 hours to reach the adsorption/desorption equilibrium. During the photocatalytic degradation reaction, 3 mL of the suspension was aliquoted every 10 min and centrifuged at 6000 rpm to separate the photocatalysts from the supernatant for analysis[65]. The concentration of RhB was calculated at the 552 nm absorption wavelength.

2.7 Electrochemical and photoelectrochemical measurements

A standard three-electrode configuration electrochemical cell with Ag/AgCl (sat. KCl) as a reference, Pt foil as a counter, and photocatalyst product coated on FTO substrate as a working electrode, were used for the electrochemical studies. 10 mg of the photocatalyst in 1 mL ethanol containing 30 µL Nafion solution 5 w/w% used to fabricate the working electrodes. The resulting suspension was irradiated with ultrasound for 30 min, and after that, 10 µL of the suspension was drop-coated on the FTO substrate and dried overnight in a vacuum oven at 50 °C. The electrochemical impedance spectroscopy (EIS) (open circuit potential: 10^5 and 10^{-2} Hz), Mott-Schottky, and chronoamperometry tests were carried out using IVIUM potentiostat/galvanostat (VERTEX entry-level instrument), at 1000 Hz frequency in −1.5 V to 1 V potential range. The photocurrent density of the as-prepared samples was measured at the set potential of 0.35 V during 220 sec with 10 sec dark and light cut-off. All of the electrochemical measurements were performed under similar conditions in a 0.5 mol/L Na_2SO_4 solution as the electrolyte.

2.8 Density Functional Theory (DFT) Methodology

To have a better understanding of the interface between CuS nanoparticles and NH_2-MIL-110(Cr), the electronic properties of CuS nanoparticles and NH_2-MIL-110-Cr and their nanocomposite were systematically calculated using density functional theory (DFT)[66,67]. The Vienna ab initio simulation package (VASP)[68,69] with the generalized gradient approximation of Perdew, Burke, and Ernzerhof (PBE)[70] were performed for all calculations. The electron-ionic core interactions were described by the Projector augmented wave (PAW) potentials[71]. Since other studies show that the inclusion of the dispersive Van der Waals forces improves the

197 energy description of the system[72], we have employed the method of Grimme, DFT-D3[73]. To
198 compute the acceptable bandgap energy consistent with the experiment, the PBE0[74] hybrid
199 functional was employed, which is implemented in the VASP code, as the literature has already
200 shown that this functional predicts more accurate band gaps for Metal-Organic Frameworks
201 (MOFs)[75]. Since the most stable surface of CuS nanoparticles is the CuS(001) with Cu/S
202 termination, which is the dominant surface observed on hexagonal-shaped CuS nanoparticles[76],
203 we have investigated the interaction of the CuS (001) surface with NH_2-MIL-110(Cr). Brillouin
204 zone integrals were approximated using the Monkhorst-Pack[77] scheme with the k-point density
205 grid of 11×11×1 for the structural and density of state (DOS) calculations. A plane-wave cutoff
206 energy of 560 eV was used. The geometry optimization was stopped when the total energy
207 converged to within 10^{-5} eV, and the force on each ion was less than 0.01 eV/Å. To avoid
208 interactions between periodic images, a vacuum space of more than 20 Å was set. The CuS(001)
209 surface was modeled by a 4×4 supercell to make sure the cell is big enough to support NH_2-MIL-
210 110(Cr) on top of the surface without interactions between periodic images. We have relaxed the
211 NH_2-MIL-110(Cr) and the two top layers of the CuS(001) surface.

212 ## 3. Result and discussion

213 ### 3.1 Characterization of NM@CuS composites

214 The PXRD patterns of the pure NH_2-MIL-101(Cr), the composite series, and pure CuS are
215 presented in Figure 1. The peak positions and diffraction intensities of NH_2-MIL-101 match the
216 observed patterns, as well as the simulated XRD for MIL-101(Cr),, reported in the
217 literature[63,78,79]. The PXRD patterns of the CuS nanoparticles confirm the presence of CuS in
218 the structure of the obtained composite samples. The main peaks of CuS nanoparticles appeared

at 2θ = 28°, 29°, 30°, 48°, 52°, and 58°. In the composite structures, both the NH_2-MIL-101(Cr) and CuS PXRD patterns are superimposed, which confirms the presence of both components in the final product. All composite samples show the same FT-IR spectra for functional peaks of NH_2-MIL-101(Cr) (Figure S1). The SEM images of the pure NH_2-MIL-101(Cr), pure CuS, and NM@CuS composite samples are shown in Figure 2. In order to determine the ratio of Cr, Cu, and S in the samples, EDX elemental analysis was carried out; The obtained data are shown in Table S1.

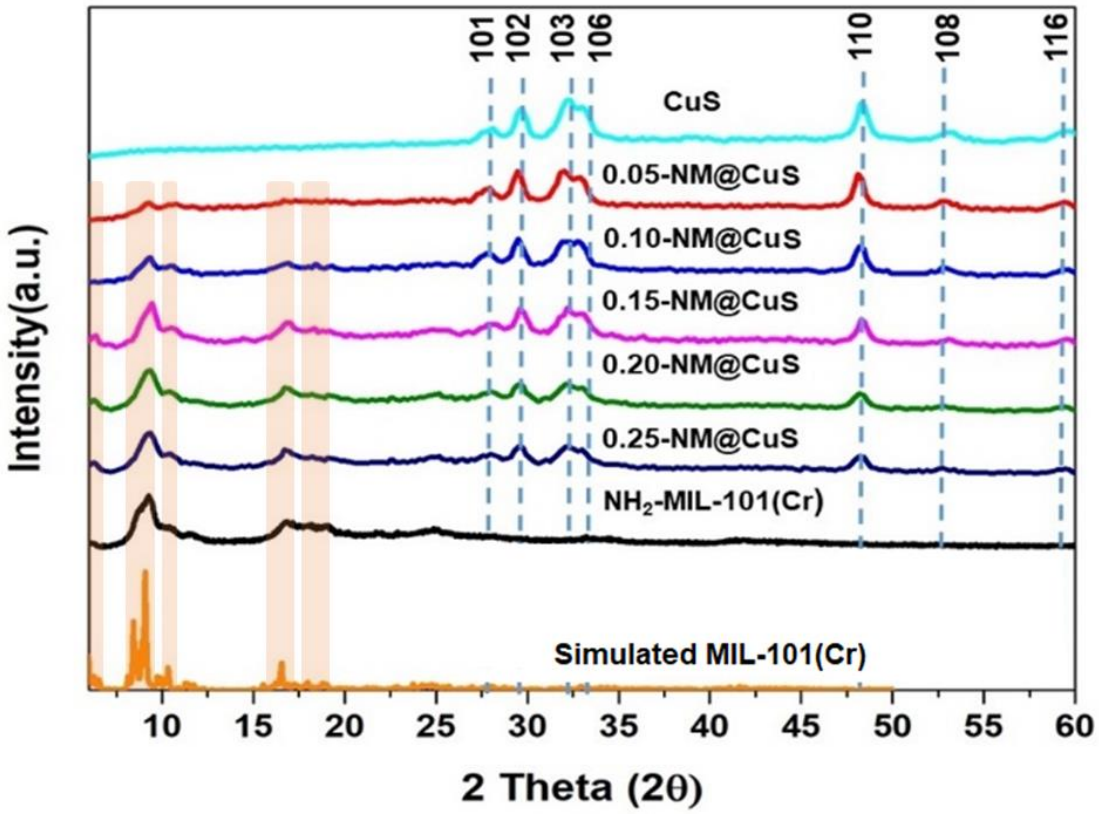

Figure 1. PXRD patterns of the as-prepared samples of NM@CuS, NH_2-MIL-101(Cr), and pristine CuS.

The calculated copper and sulfur atomic ratio (Table.S1) in the structures of the composites showed that by increasing the weight of the NH_2-MIL-101(Cr) in the initial suspension, the relative

amount of sulfur also increased. These changes in the atomic ratio of the copper and sulfur resulted from the partial reduction of copper cations by carboxylic acid groups in the structure of NH_2-MIL-101(Cr). The same phenomenon has been detected in the presence of some other reducing agents in the reaction media[80,81].

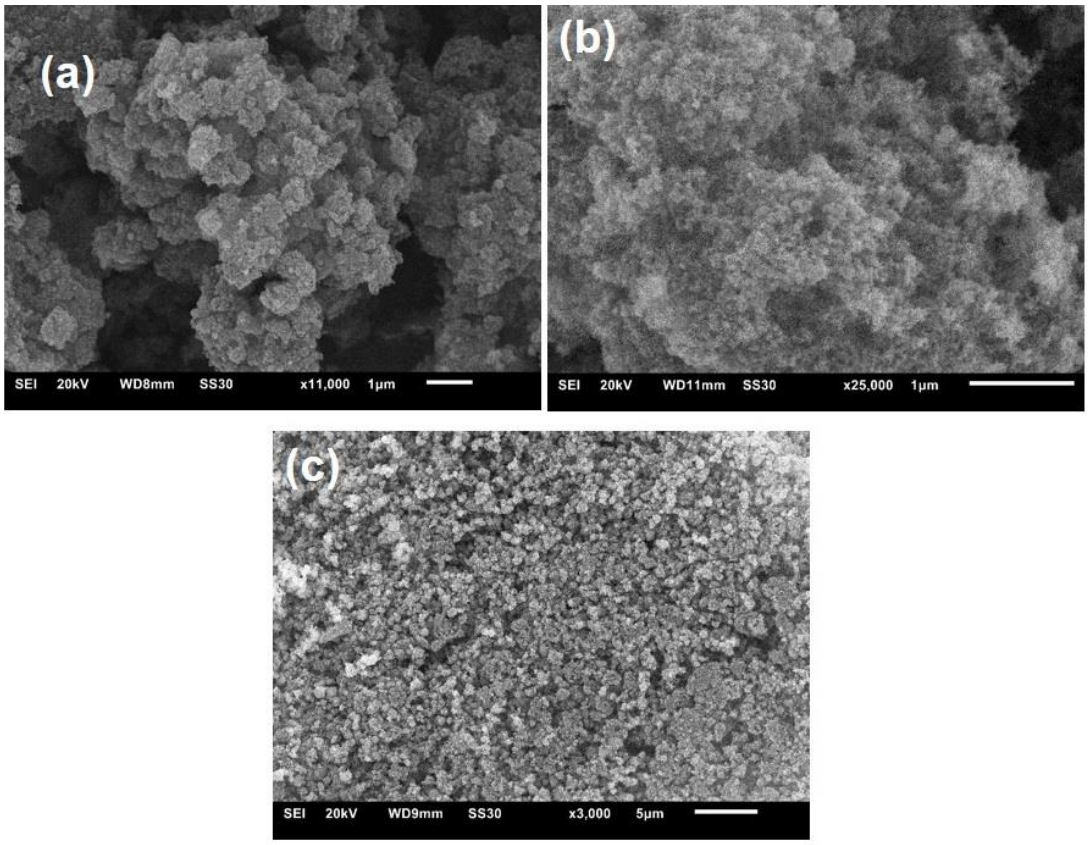

Figure 2. SEM images of (a) NH_2-MIL-101(Cr), (b) CuS nanoparticles, (c) NM@CuS composite.

As seen in the HR-TEM images (Figure 3), the CuS nanoparticles, which had an average size of about 44 nm, can be distinguished from NH_2-MIL-101(Cr) (average size about 55 nm) by darker and egg-shaped morphologies.

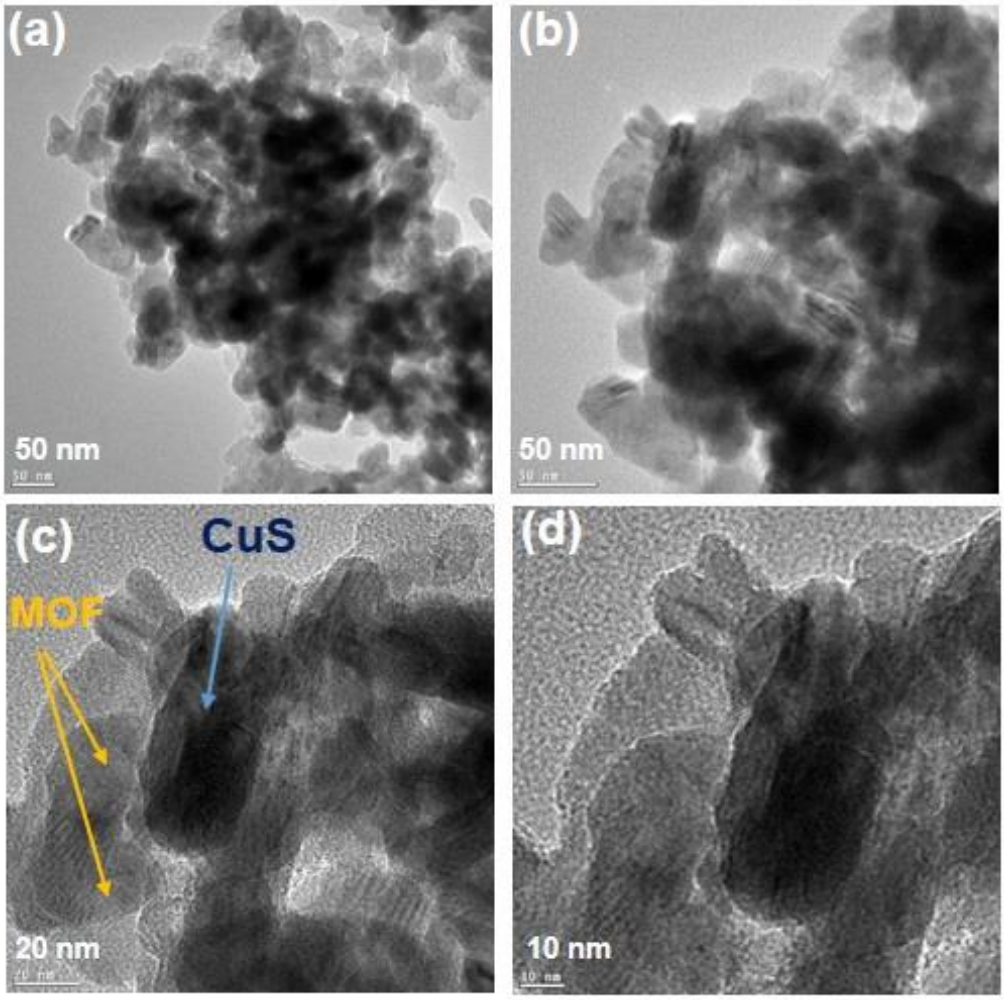

241

242 **Figure 3.** (a,b,c,d) HR-TEM images of the 0.15-NM@CuS in different magnitude.

243 In order to identify the phase of the CuS nanoparticles, SAED was used for four different areas
244 on the TEM-grid, which supports the hexagonal space group of the CuS nanoparticles, whereas
245 the diffraction rings match the literature value (hexagonal, space group P63/mmc, COD: 9008389).
246 (Figure 4)[82,83].

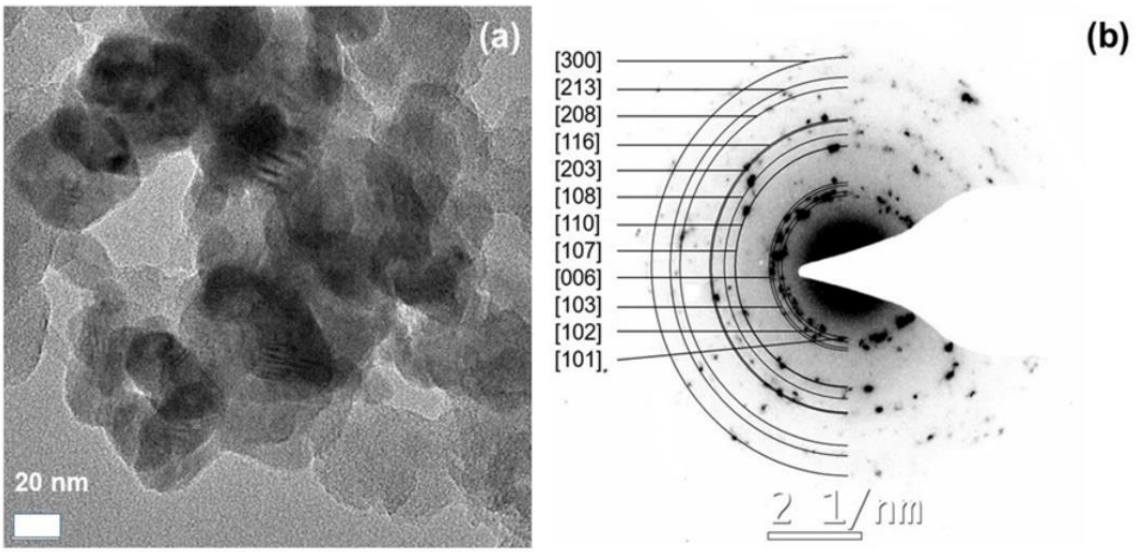

247

248 **Figure 4.** Selected-area electron diffraction (SAED) patterns of 0.15-NM@CuS (diffraction rings
249 for hexagonal CuS, space group $P6_3/mmc$, COD: 9008389).

250 Figure 5 presents nitrogen adsorption-desorption isotherms of the as-prepared activated
251 NH_2-MIL-101(Cr) and composite samples, which all demonstrated the same type I isotherms due
252 to their microporous structure[63]. By increasing the weight fraction of CuS nanoparticles in the
253 final samples, the surface area, along with the total pore volume, was reduced. The total pore
254 volume and surface area of the samples are exhibited in Table 1.

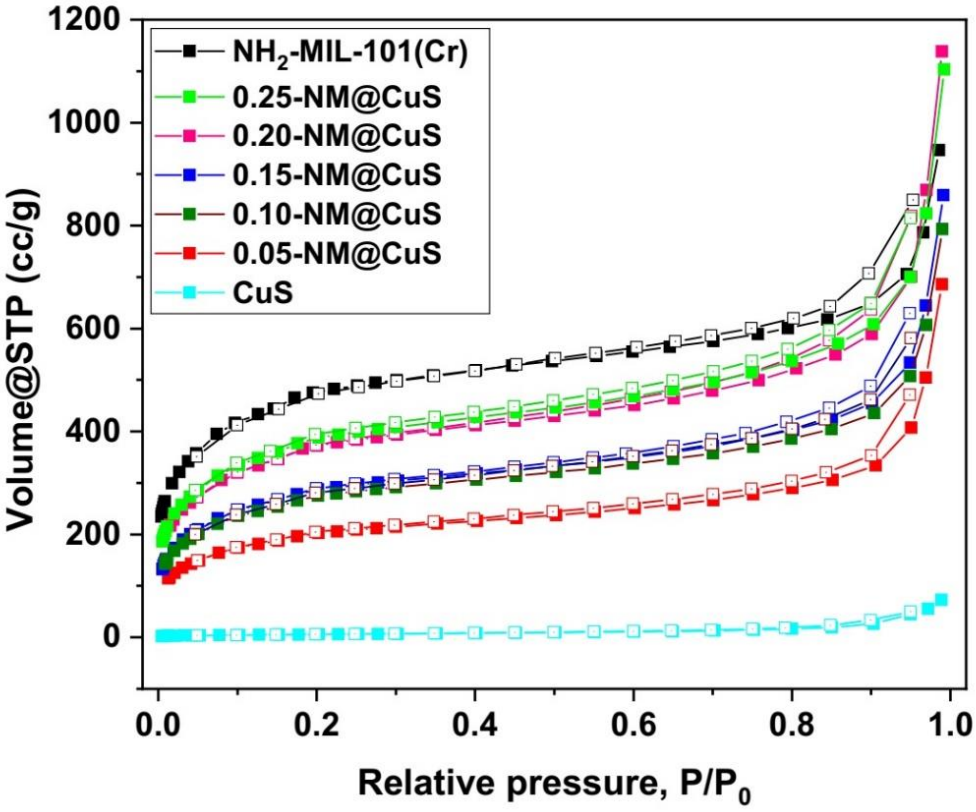

255

256 **Figure 5.** Nitrogen adsorption-desorption isotherms at 77 K of the as-prepared samples. The filled

257 and empty symbols represent adsorption and desorption, respectively.

258

259

260

261

262

263

Table 1. Surface area and pore volume values of the as-prepared samples.

Sample	BET surface area (m^2/g) [a]	Total pore volume (cm^3/g) [b]
NH_2-MIL-101 (Cr)	1732	0.52
0.25-NM@CuS	1411	0.38
0.2-NM@CuS	1351	0.33
0.15-NM@CuS	1041	0.27
0.1-NM@CuS	996	0.25
0.05-NM@CuS	739	0.09
CuS	21	0.01

[a] Calculated BET surface area from N_2 adsorption isotherms at 77 K over a pressure range of $P/P_0 = 0.05$ -0.4.
[b] Total pore volume at $P/P_0 = 0.95$ for pores ≤ 37 nm.

The XPS of the as-prepared 0.15-NM@CuS was employed to elucidate the chemical composition of the elements at the surface, considering the chemical environment of the CuS nanoparticles and NH_2-MIL-101(Cr) in the structure of the composite samples. The presence of Cu, Cr, S, N, C, and O in the as-prepared 0.15-NM@CuS was confirmed by the survey spectrum of the composite structures (Figure 6a).

The Cr $2p_{3/2}$ orbital indicates two different Cr^{3+} species. The Cr^{3+} species at 575.6 eV can be ascribed to Cr–OH_2 and the other species at 578.0 eV can be ascribed to Cr–OH. The ratios of about 2:1 correspond to the trinuclear Cr_3 unit with two bound aqua ligands and one hydroxide ligand in NH_2-MIL-101(Cr) (Figure 6b)[84]. The high-resolution spectrum of the Cu 2p (Figure 6c) shows two prominent peaks at 933.3 and 953.0 eV, which can be ascribed to Cu $2p_{3/2}$ and Cu $2p_{1/2}$ in the structures of the CuS nanoparticles, whereas the small peak around 933.3 eV can be

attributed to impurities of Cu^{+} with the central peak at 933.5 eV ascribed to Cu^{2+}. The S 2p peak confirmed these results[85]. Furthermore, the S 2p peak (Figure 6d) located at 163.5 eV, which splits into two peaks at 163.1 and 164.9 eV, corresponds to $S2p_{3/2}$ and $S2p_{1/2}$ which confirms the presence of sulfur metal in the structure of the NM@CuS composite materials[36,86].

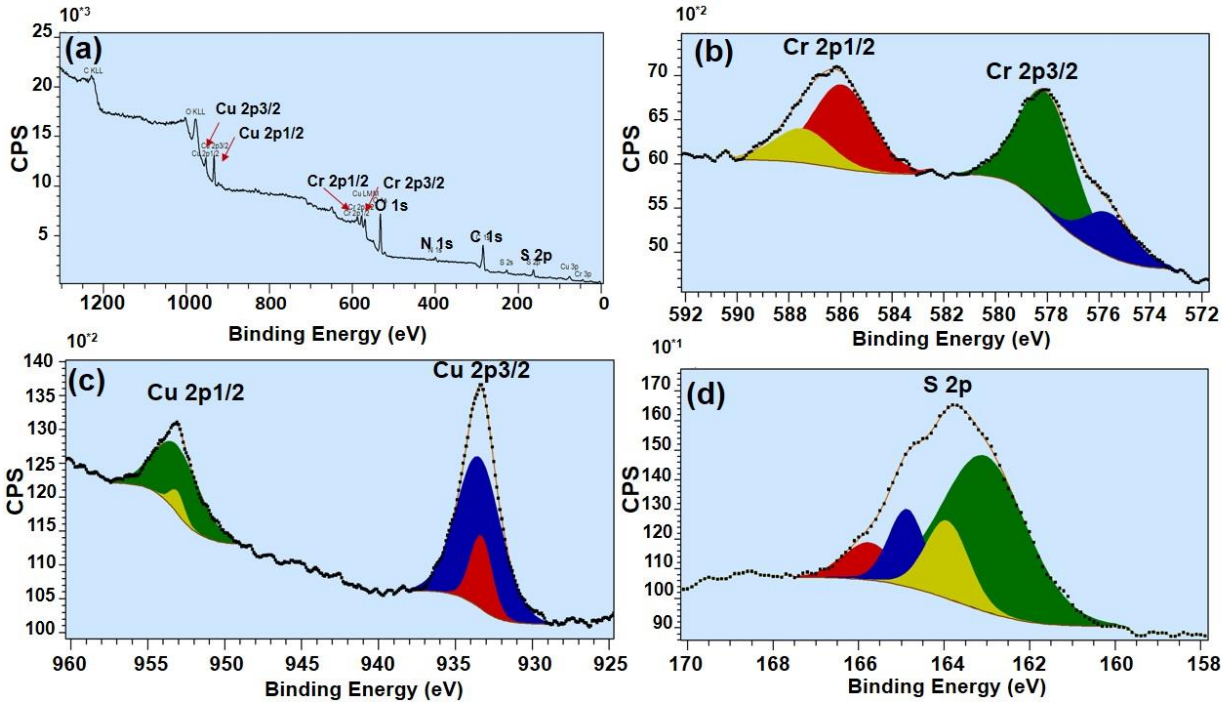

Figure 6. XPS spectra of the 0.15-NM@CuS (a) survey spectrum, (b) Cr 2p, (c) Cu 2p, (d) S 2p region from high-resolution XPS.

The C1s, N1s, and O 1s peaks are shown in Figure S2, Figure S3, and Figure S4, respectively, with the XPS analysis data shown in Table S2. All of the XPS data confirmed the presence of the NH_2-MIL-101(Cr) and CuS in the structure of the composite samples.

The optical properties of the samples were determined by diffuse reflectance spectroscopy (DRS). Figure 7a shows the UV-Visible absorption behavior of the as-prepared samples. The adsorption band position of the NH_2-MIL-101(Cr) in the UV region was ascribed to π-π^* of the

ligand[87], while the low adsorption band around 600 nm can be related to the d-d spin-allowed transition of Cr^{3+} centers[56]. The UV-visible light spectrum of the composite photocatalysts, NM@CuS, indicates that the visible light absorption intensity is significantly higher than in pure NH_2-MIL-101(Cr), which can be attributed to intensive absorption of UV-Visible light by the CuS nanoparticles in the NM@CuS structures. Also, broadband extending into the near-IR region indicates the presence of CuS nanoparticles in the as-obtained composite photocatalyst materials[88].

The optical band gap energy of the samples was determined using the intercepts of the tangents of $(Ahv)^2$ vs. (hv) (tauc plot), shown in Figure 7b for each sample.

$$\alpha(hv) = A\,(hv - E_g)^{1/2}$$

Where α is the absorption coefficient, v is the light frequency, E_g is the semiconductor bandgap energy, and A is the equation constant, respectively.

Thus, the band gaps of the samples were estimated from intercepts of the above equation as 1.8 (Fig.S8), 1.98, 2.05, 2.19, 2.25, 2.30, and 2.6 eV for CuS, 0.05-NM@CuS, 0.10-NM@CuS_y, 0.15-NM@CuS, 0.20-NM@CuS, 0.25-NM@CuS, and NH_2-MIL-101(Cr), respectively. The band gap values show that the optical band gap of the composite samples increases with the increasing amount of the MOF in the structures of the composites.

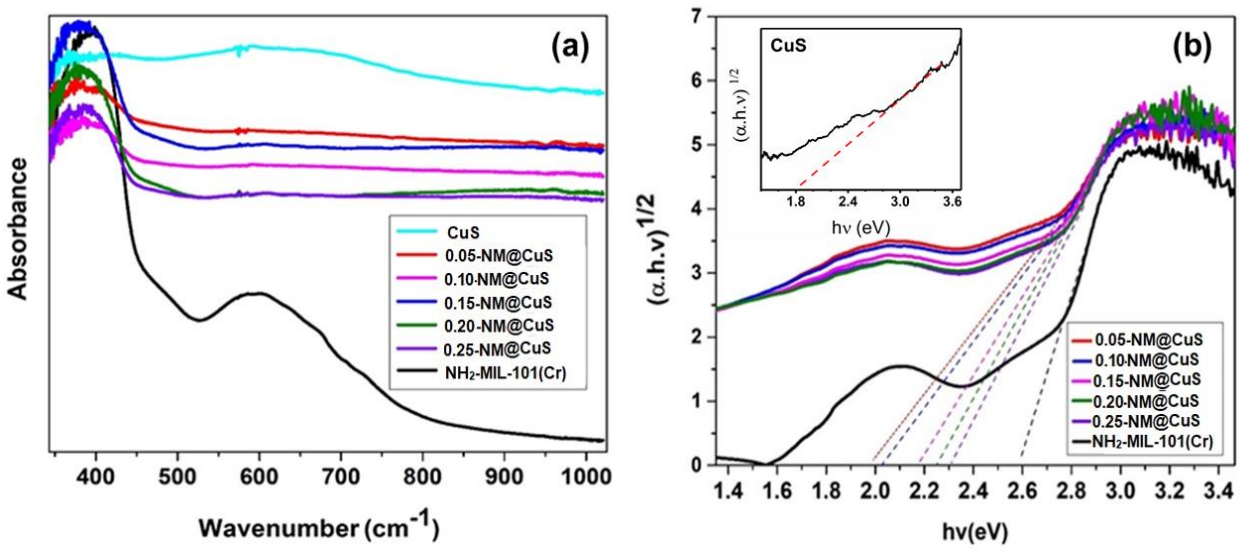

311

312 **Figure 7.** (a) UV-visible absorption spectra of the as-prepared samples, (b) plot of $(\alpha h\nu)^{1/2}$ versus

313 energy ($h\nu$) for the bandgap energy of the samples.

314 **3.2 Photocatalytic degradation of RhB**

315 The photocatalytic performance of the as-prepared samples was evaluated via the degradation of

316 model polluted water with RhB dye (10 ppm, pH = 7.0. room temp) under visible light irradiation

317 (Xenon lamp 500 W). As shown in Figure 8a, in the absence of the photocatalyst, no significant

318 RhB degradation was observed. The concentration of RhB decreased by increasing the irradiation

319 time, and all samples showed higher degradation performance compared to the individual parent

320 materials.

321 Maximum photocatalytic degradation (C/C_0 = 0.06) was observed when the 0.15-NM@CuS

322 sample was used. The photocatalytic activity of the samples was increased by increasing the

323 number of NH_2-MIL-101(Cr) nanoparticles in the structure of the final composite samples, and it

324 reached the maximum at 0.15 g of the NH_2-MIL-101(Cr) in the precursor suspension. Next, further

325 increasing the NH_2-MIL-101(Cr) loading in the nanoparticles caused a decline in the

photocatalytic performance, although it was still better than pure NH_2-MIL-101(Cr) and CuS nanoparticles. Two phenomena lead to maximum photocatalytic activity in a certain loading amount of NH_2-MIL-101(Cr) nanoparticles, relating to a change in the UV-Visible light absorption and the bandgap properties of the composite samples.

The UV-visible absorption spectra of the samples (Figure 7a) indicate that the absorption rate above 450 nm becomes more potent when the loading of NH_2-MIL-101(Cr) nanoparticles decreases, which leads to significant absorption of visible light and excitation of more electron-hole pairs. Alternatively, the bandgap of the composite samples decreases with increasing loading of the copper sulfide nanoparticles that reduce the photocatalytic performance by increasing the electron-hole recombination rate[89].

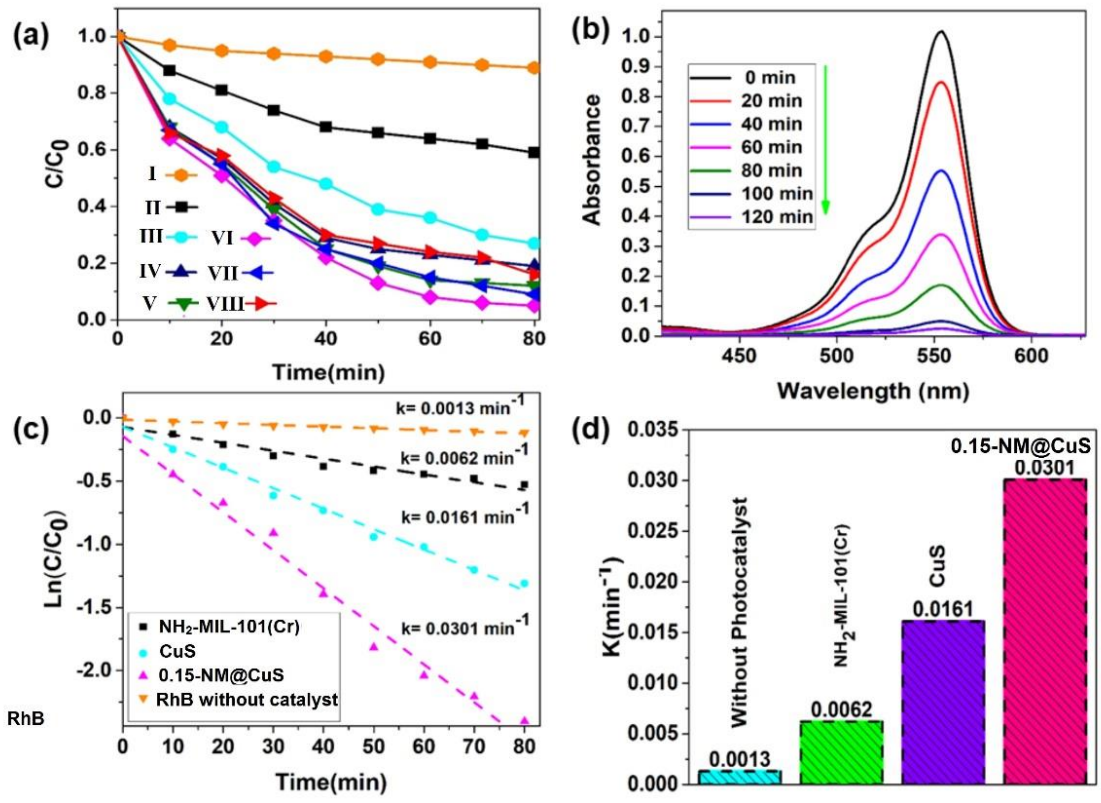

Figure 8. (a) photocatalytic degradation rate of RhB under visible-light irradiation (>420 nm) without and in the presence of the photocatalyst samples. (I) without catalyst, (II) NH_2-MIL-101(Cr), (III) CuS, (IV) 0.05-NM@CuS, (V) 0.10-NM@CuS, (VII) 0.20-NM@CuS, (VI) 0.15-NM@CuS, (VIII) 0.25-NM@CuS (b) RhB absorption spectra in the presence of 0.15-NM@CuS_y in different irradiation times (c), natural logarithm C/C_0 fitting curves of NH_2-MIL-101(Cr), CuS, 0.15-NM@CuS and without photocatalyst (d), the value of the rate constant k of the photodegradation process of RhB.

Parameters such as the increase in the UV-visible absorption; decrease in the bandgap energy levels as the amount of NH_2-MIL-101(Cr) nanoparticles decreases; and also the effect of changing the surface area of the samples by altering the NH_2-MIL-101(Cr) loading; lead to a boost in the photocatalytic activity by loading NH_2-MIL-101(Cr) nanoparticles up to 0.15 g in the composite structures. The sulfur enrichment in the NM@CuS samples can also enhance the photocatalytic performance of the samples, as is already reported for photocatalysts containing copper-sulfur nanoparticles[80,90].

The change with time in the absorption spectra of RhB in the UV-visible region in the presence of 0.15-NM@CuS product is also shown in Fig. 8b. As seen in this figure, the main peak at 554 eV diminishes with time over the reaction. A kinetic study of the photocatalytic reaction is performed by fitting the experimental data for NH_2-MIL-101(Cr), CuS, and 0.15-NM@CuS, by using a first-order model applying the following equation:

$$-Ln(C/C_0) = kt$$

where C_0 is the RhB concentration at equilibrium after a 2-hour adsorption/desorption process in dark conditions, C is the residual RhB concentration at time t (min) in the solution, and k is the apparent rate constant in the first-order kinetic model. As indicated in Figure 8 c,d the apparent constant (k) for the 0.15-NM@CuS is 1.87 times more than CuS and also 4.85 times more than NH_2-MIL-101(Cr). The higher apparent constant (k) of the 0.15-NM@CuS compared to pure NH_2-MIL-101(Cr) and CuS nanoparticles confirm the more effective photodegradation of RhB in the presence of 0.15-NM@CuS.

In Figure 9a, the effect of raising the concentration of RhB on the photocatalytic performance of the samples is plotted. The maximum photocatalytic activity is observed when the initial concentration of RhB was 5 ppm (in the presence of 0.15-NM@CuS). As the RhB dye concentration increase, the photocatalytic activity reduces, which can be linked to the reduction in numbers of photons hitting the photocatalyst surfaces through extending the visible-light absorption by the dye molecules at the catalyst surfaces and in the solution[91].

The outcome of increasing the amount of photocatalyst on the photodegradation of RhB was also explored. By increasing the amount of photocatalyst (0.15-NM@CuS) from 5 mg to 40 mg, the degradation of RhB was boosted, but when the amount of photocatalyst is over 80 mg, the degradation was diminished (Figure 9b), which could be the result of shielding effects of the high concentration of photocatalyst particles that inhibit the light reaching other photocatalyst particles in the suspension[92].

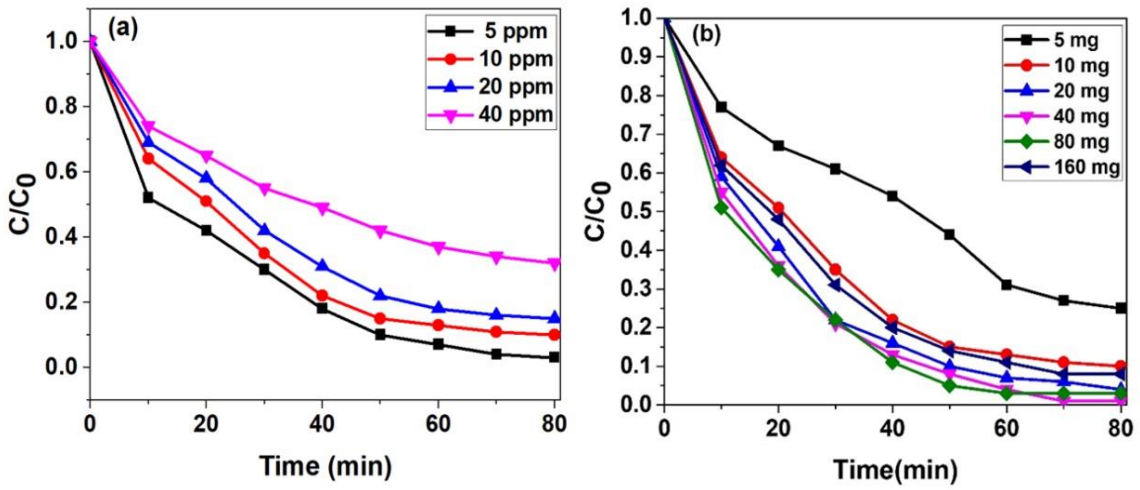

377

378 **Figure 9.** (a) Effect of different RhB concentrations on the photocatalytic performance of 0.15-
379 NM@ CuS, (b) effect of photocatalyst dosage on photocatalytic degradation of RhB.

380 The stability of the photocatalyst (0.15-NM@CuS) was evaluated by 4-time cycles of the
381 photocatalytic reaction. After each cycle, the photocatalyst was washed and dried for the next
382 cycle. As presented in Figure 10, after 4 cycles, about 89% of the RhB can be degraded, which
383 shows the solidity of the photocatalyst during the cyclic photocatalytic reaction. The reduction of
384 RhB can be attributed to a partial loss of the photocatalyst through the washing procedure of cycles
385 of the photocatalytic reaction. The reusability experiment and also PXRD (Figure S5) and FT-IR
386 spectra (Figure S6) of the photocatalyst sample after the cyclic experiment prove the stability of
387 the as-prepared composite sample during the photocatalytic reaction. The ICP-mass spectroscopy
388 (Table S3) was also used to determine the concentration of probable leached Cr^{3+} in the solution
389 resulting from the MH_2-MIL-101(Cr). The ICP-mass data revealed that no significant Cr^{3+} existed
390 in solution, which confirms the stability of the MOF structure in the aqueous solution as the
391 catalytic reaction proceeds.

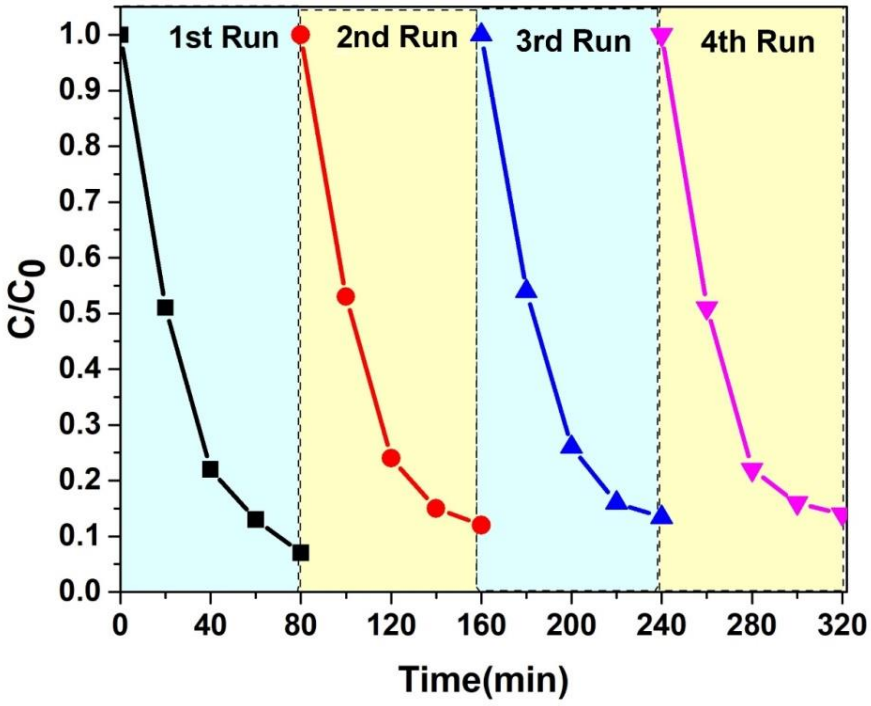

392

393 **Figure 10.** Cycling runs of the photocatalytic degradation of RhB (10 ppm) over 0.15-NM@CuS.

394

395 **3.3 Photocatalytic degradation mechanism of RhB over NM@CuS**

396 In the photocatalytic degradation process of organic impurities in water, three active species play
397 an essential role, including superoxide radicals ($\bullet O_2^-$), holes (h^+), and hydroxyl radicals (•OH),
398 which depending on the type of photocatalytic reaction, play different roles in the overall
399 photocatalytic reaction. To determine the main active components in the photocatalytic
400 degradation process of RhB, a trapping experiment was conducted (Figure 11). Three different
401 scavengers, benzoquinone (BQ, 0.05 mM), ammonium oxalate (AO, 0.05 mM), and tert-butyl
402 alcohol (TBA, 0.05 mM), were used as an anion radical ($\bullet O_2^-$) scavenger, hole (h+) scavenger, and
403 photogenerated hydroxyl radical (•OH) scavenger, respectively[93].

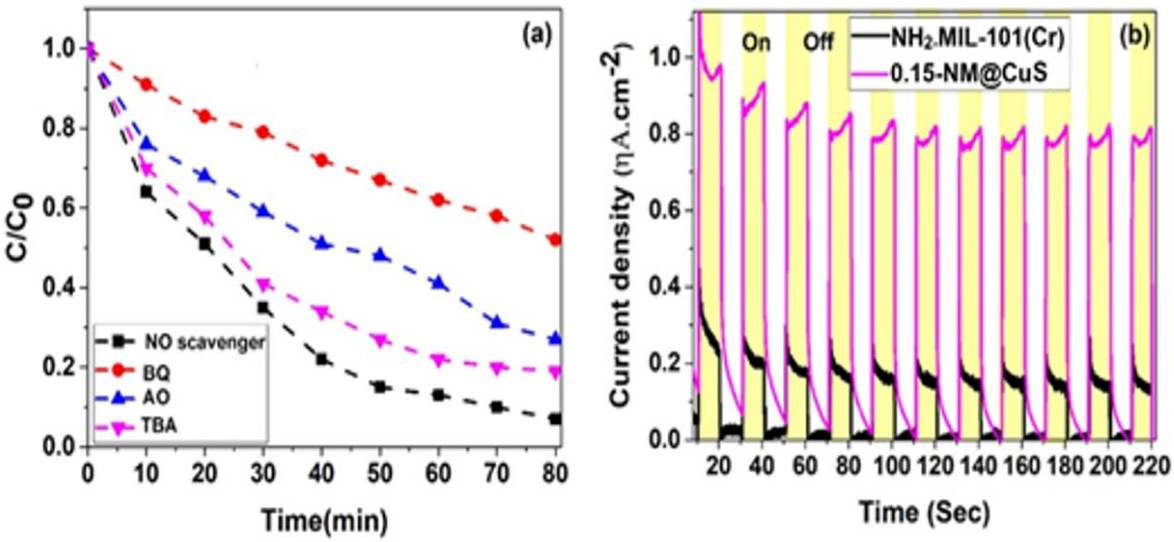

404

405 **Figure 11** (a) Photocatalytic activity of the 0.15-NM@CuS for the degradation of RhB in the
406 presence of different scavengers, (b) Transient photocurrent response of the pure
407 NH_2-MIL-101(Cr) and 0.15-NM@CuS.

408

409 As shown in Figure 11a, the photodegradation of RhB dramatically decreased over an 80 min
410 reaction time (C/C_0= 55) in the presence of BQ compared to the absence of scavenger
411 (C/C_0 = 0.06). This shows that the superoxide radicals ($^{\bullet}O_2^-$) formed through the direct reaction of
412 photogenerated electrons with the adsorbed oxygen molecules on the surface of the photocatalyst
413 play an essential role in the photodegradation of RhB in the presence of NM@CuS. Also, adding
414 a hole (h+) and hydroxyl radical ($^{\bullet}OH$) scavenger decreased the photocatalytic degradation of RhB
415 to about (C/C_0 = 0.27) and (C/C_0= 0.19), respectively. The obtained data from trapping
416 experiments revealed that scavengers for the superoxide radical ($^{\bullet}O_2^-$), the hydroxyl radical ($^{\bullet}OH$),
417 and holes (h^+) affect the photodegradation process in the presence of NM@CuS, but the superoxide
418 radical ($^{\bullet}O_2^-$) plays a substantial role in the photocatalytic response. In contrast, the hydroxyl

radical (•OH) has a less critical role. As such, the photocatalytic performance of a photocatalyst composite is directly related to the transfer rates of photogenerated electrons and holes during the photocatalytic reaction.

The photocurrent density of the pure NH_2-MIL-101(Cr) and 0.15-NM@CuS (as the best photocatalytic sample) was also reported in Figure11b. The higher photocurrent density found for the 0.15-NM@CuS (0.8 $\mu A/cm^2$) sample compared to NH_2-MIL-101(Cr) (0.2 $\mu A/cm^2$) confirms the higher photogenerated electron and hole transfer rate in the composite samples compared to pure NH_2-MIL-101(Cr), which can be associated with active electron and hole transfer between CuS and NH_2-MIL-101(Cr) in the composite sample[94].

Next, the photoluminescence (PL) spectra of the samples were determined (Figure S7). The 0.15-NM@CuS sample showed a lower PL spectrum intensity, which relates to sufficient hole and electron separation in the structure of the 0.15-NM@CuS compared to other samples. These results are consistent with the obtained data from transient photocurrent and photocatalytic studies.

With the intention of further understanding of charge carrier migration, EIS was recorded and presented as a Nyquist plot (Figure 12a). The small semicircle Nyquist plots of 0.15-NM@CuS compared to NH_2-MIL-101(Cr) and CuS can be ascribed to faster electron-hole migration in the composite sample compared to the parent materials, which is consistent with the photocurrent result[95].

To further study the electrochemical behavior of the photoelectrodes, the simulated circuit of the electrochemical cell was calculated, and the electron lifetime of the 0.15-NM@CuS, NH_2-MIL-101(Cr), and CuS was estimated from a Bode plot. The corresponding parameters calculated for the equivalent circuit are presented in Table.2. The equivalent circuit consisted of

two parallel R_C and C_{dl} elements along with the Warburg impedance (Zw) used to fit the data (Fig.12a inset). As shown in Figure 12a, FTO sheet resistance (Rs) is represented by a non-zero intercept on the real axis in the EIS plot. R_{CE} is the resistance of the electrode at the electrolyte interface, and R_{CT} is the resistance due to the charge transfer at the interface of the photoelectrode with the electrolyte. The electron lifetime was also calculated from the peak angular frequency value, which shows a higher value for 0.15-NM@CuS compared to NH_2-MIL-101(Cr) and CuS, thereby confirming the effective electron-hole separation in the composite sample[96].

The electron lifetimes are calculated from the peak angular frequency value (f_{max}) using the following equation:

$$\tau_n = \frac{1}{2\pi f_{max}}$$

A higher τ_n value reveals that the electrons have an extended lifetime and transferred efficiently, resulting in higher photocurrent density with elevated energy conversion efficiency.

Table 2. the electrochemical parameters of the as-prepared photocatalytic electrode derived from the simulated circuit.

Sample	R_S (Ω)	R_{CT} (Ω)	C_{dl} (μF)	Z_W (μΩ)	τ_n (ms)
CuS	117.6	0.005	11.98	15.57	0.2
NH_2-MIL-101 (Cr)	105.6	5.65	4.79	25.44	0.2
0.15-NM@CuS	82.8	0.034	5.16	43.92	3.3

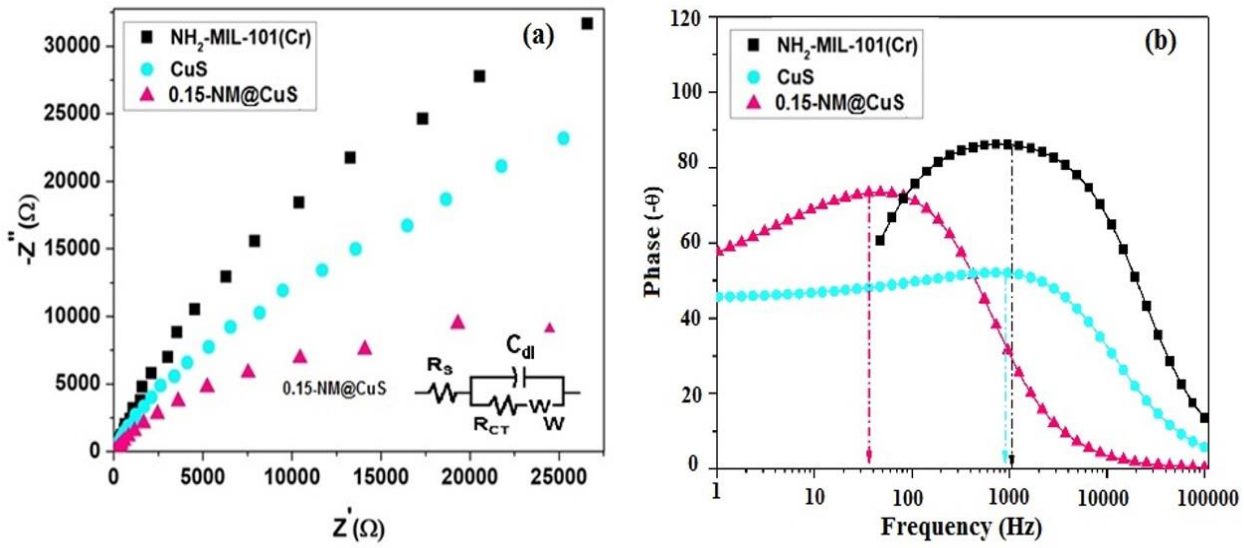

456

457 **Figure 12.** (a) EIS property (Nyquist plot) of NH_2-MIL-101(Cr), CuS, and 0.15-NM@CuS
458 composites (b) bode plot of the of NH_2-MIL-101(Cr), CuS, and 0.15-NM@CuS composite.

459 To determine the flat band potential of the NH_2-MIL-101(Cr) and CuS, Mott-Schottky analysis
460 was used[97]. The positive slope of the Mott-Schottky plot (Figure 13a) for NH_2-MIL-101(Cr)
461 and a negative slope for the CuS nanoparticles (Figure 13b) revealed the n-type and p-type
462 properties of the MIL-101(Cr) and CuS nanoparticles, respectively[98]. As shown in Figure 13
463 (a,b), the flat band potentials (vs. Ag/AgCl) for NH_2-MIL-101(Cr) and CuS nanoparticles are
464 located at -0.6 V and 0.85 V, respectively. The flat band potentials can be converted into normal
465 hydrogen electrode potential (NHE) according to the following equation ($E^{\circ}_{Ag/AgCl} = 0.197$ V):

466 $$E_{NHE} = E_{Ag/AgCl} + E^{\circ}_{Ag/AgCl}$$

467

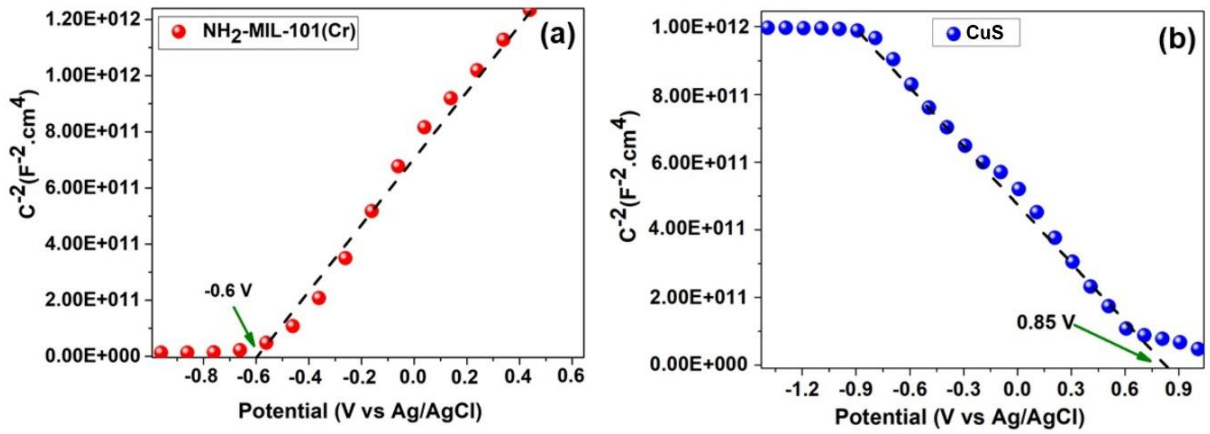

468

469 **Figure 13.** Mott-Schottky plots of pure NH_2-MIL-101(Cr) and CuS.

470 It is commonly accepted that the potential of the conduction band (CB) is 0.1 V above the flat
471 band in an n-type semiconductor, and the potential of the valence band (VB) is 0.1 V below the
472 flat band potential in a p-type semiconductor[99]. Hence, the CB of NH_2-MIL-101(Cr) and VB of
473 CuS are -0.503 and 1.147 V (vs. NHE), respectively, with band gap potentials of 2.6 eV for NH_2-
474 MIL-101(Cr) and 1.8 eV for CuS. Thus, the VB and CB potential of NH_2-MIL-101(Cr) and CuS
475 are calculated as 2.097 eV and -0.653 eV, receptively.

476

477 ### 3.4. Results from DFT Calculations

478 The optimized cell parameters for CuS bulk were a = 3.782 Å and c = 16.290 Å, i.e. in excellent
479 agreement with the experiment (a = 3.794 Å and c = 16.341 Å)[100] and previous ab initio studies
480 (a = 3.791 Å and c = 16.400 Å)[76]. Geometries of the relaxed CuS bulk, CuS(001) surface, NH_2-
481 MIL-110(Cr), and NH_2-MIL-101(Cr)@CuS(001) nanohybrid photocatalysts used in our
482 calculations are shown in Figure 14.

The thermodynamic stability of the NH_2-MIL-101(Cr)@CuS(001) composite can be investigated by calculating the binding energy using the following equation:

$$E_b = E_{\mathrm{NH2-MIL-101(Cr)@CuS(001)}} - E_{\mathrm{CuS(001)}} - E_{\mathrm{NH2-MIL-101(Cr)}}$$

Where $E_{\mathrm{NH2-MIL-101(Cr)@CuS(001)}}$, $E_{\mathrm{CuS(001)}}$ and $E_{\mathrm{NH2-MIL-101(Cr)}}$ represent the total energies of the NH_2-MIL-101(Cr)@CuS(001) nanohybrid, the CuS(001) surface, and the NH_2-MIL-101(Cr), respectively. The calculated E_b is -3.85 eV for the NH_2-MIL-101(Cr)@CuS(001), which shows the stability of the hybrid structure thermodynamically, compared to its components.

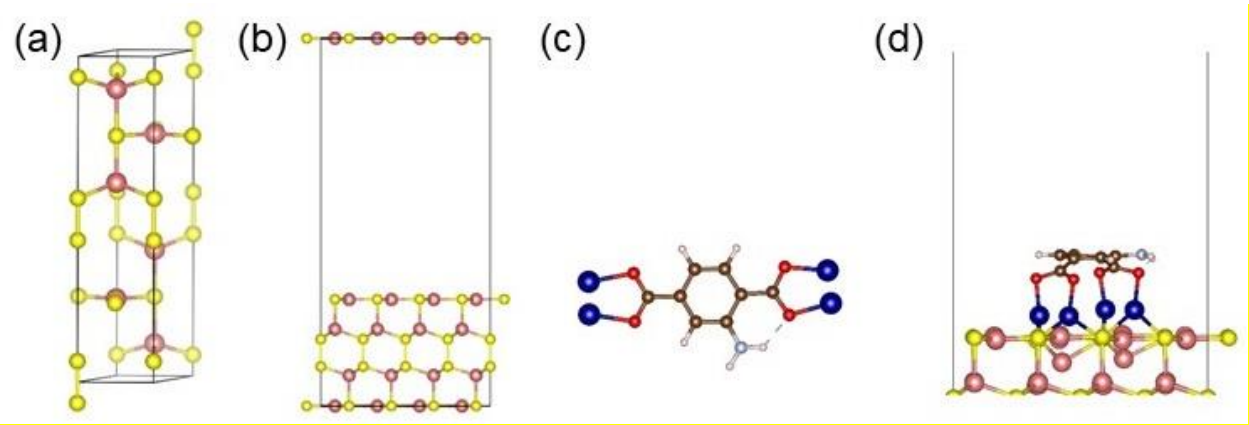

Figure 14. Geometries of (a) CuS bulk, (b) CuS(001) surface, (c) NH_2-MIL-101(Cr) and (d) NH_2-MIL-101(Cr)@CuS(001) interface after optimization. Colors of Cu, S, O, N, H, C, and Cr atoms are pink, yellow, red, silver, white, brown, and blue, respectively.

To explore the nature of the interaction between NH_2-MIL-101(Cr) and the CuS (001) surface, electronic structure calculations of the NH_2-MIL-101(Cr), CuS(001) surface, and

498 NH_2-MIL-101(Cr)/CuS (001) hybrid structure were carried out, and the results are shown in
499 Figures 15 and 16.

500 The calculated band structures show that the hybrid NH_2-MIL-101(Cr)/CuS(001) system has a
501 direct bandgap as large as 2.10 eV (Figure 15). The CuS(001) surface has a direct bandgap of 1.64
502 eV, shown in Figure 15b, with the valence band maximum (VBM) and the conduction band
503 minimum (CBM) located at the Γ point. Besides, the direct bandgap for NH_2-MIL-101(Cr) is 2.65
504 at X high symmetry point (Figure 15). These results are consistent with our experimental findings,
505 confirming that CuS nanoparticles are mostly composed of CuS(001) surfaces. It should be noted
506 that the smaller bandgap obtained for the hybrid structure can notably increase the photocatalytic
507 performance of NH_2-MIL-101(Cr) under visible irradiation.

508 To further study the electronic structure of the NH_2-MIL-101(Cr) and CuS(001) at the interface
509 in the hybrid system, the total DOS (TDOS) and its projected DOS (PDOS) were also calculated,
510 and the results are shown in Figure 16. According to Figure 16a, while the CBM of the NH_2-MIL-
511 101(Cr)/CuS(001) hetero-structure mainly originates from the atomic orbitals Cr(p) of the NH_2-
512 MIL-101(Cr), the VBM is dominated by the Cu(d) and S(p) orbitals of the CuS(001) surface.
513 Moreover, Figures 16b and 16c indicate that the CBM and VBM of the naked CuS(001) surface
514 and NH_2-MIL-101(Cr) semiconductor are composed of S(p) and Cr(d) orbitals, respectively.

515

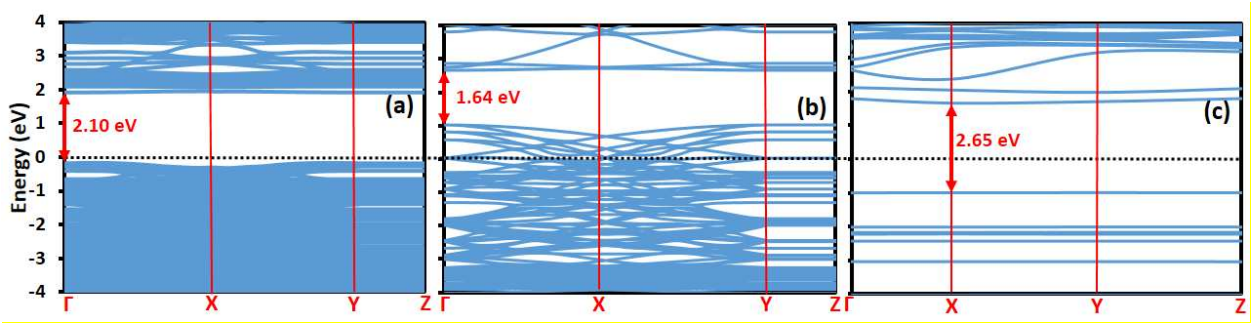

Figure 15. Calculated band structure of (a) hybrid structure NH_2-MIL-101(Cr)@CuS(001), (b) CuS(001), and (c) NH_2-MIL-101(Cr).

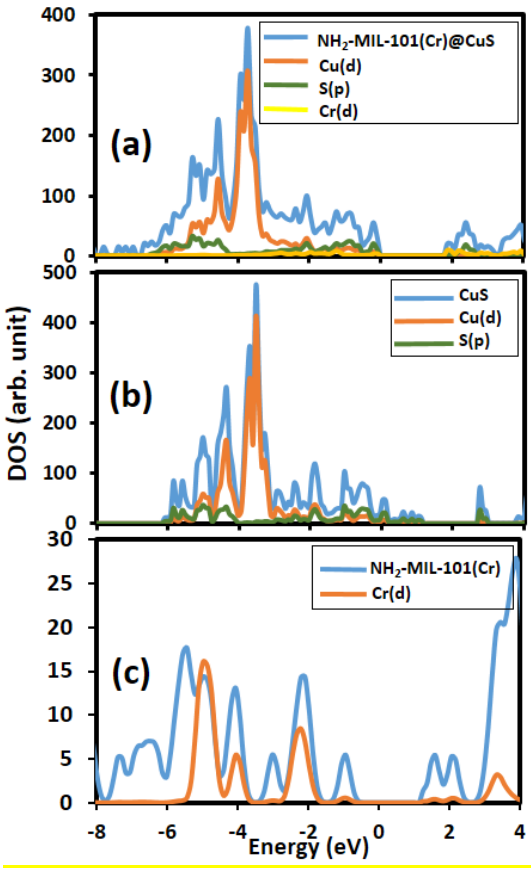

Figure 16. Calculated DOS of (a) hybrid structure NH_2-MIL-101(Cr)@CuS(001), (b) CuS(001), and (c) NH_2-MIL-101(Cr).

Taking the remarkable enhancement in charge separation based on PL and photoelectrochemical analysis, the composite photocatalyst has a direct Z-Scheme mechanism, which is shown in Scheme 1.

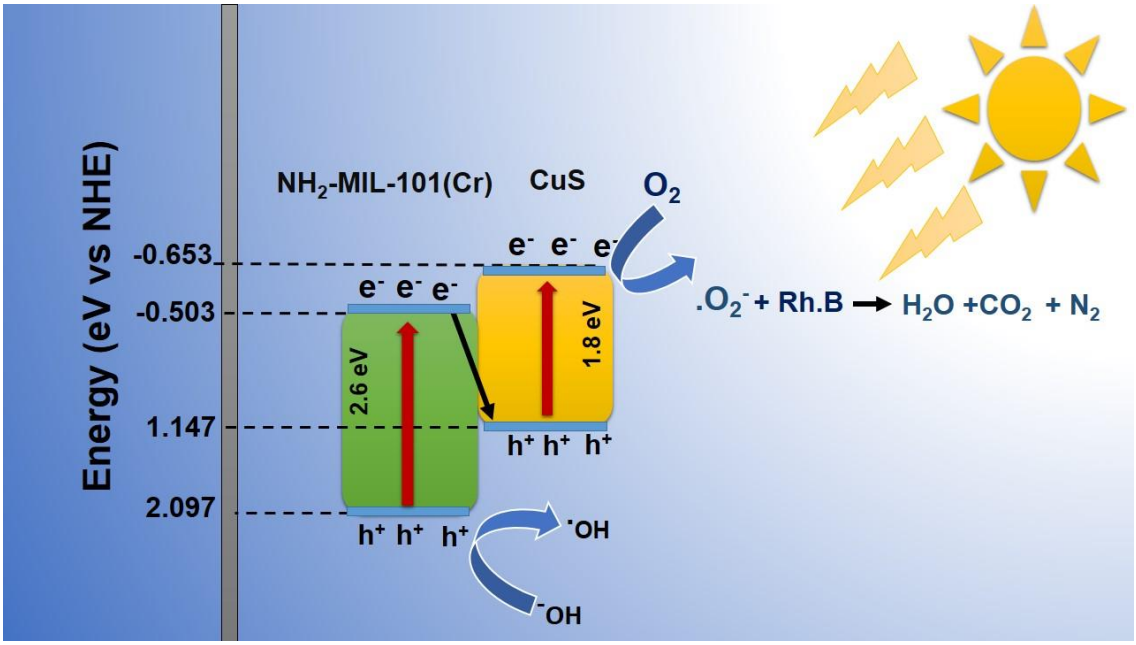

Scheme 1. Schematic illustration of the direct Z-Scheme mechanism of 0.15-NM@CuS towards the photodegradation of RhB.

Visible-light irradiation drives the electrons generated in the CuS and NH_2-MIL-101(Cr) valence bands to the conduction band through the excitation process. The photo-exited electrons in the conduction band of NH_2-MIL-101(Cr) at -0.503 V (vs. NHE) react with holes in the valence band of CuS and at 1.147 V (vs. NHE). The trapping experiment revealed that the main active species were superoxide radicals ($\bullet O_2^-$). Therefore, the adsorbed O_2 molecules on the surface of the photocatalyst can be reduced by electrons in the CB of NH_2-MIL101(Cr) to create the superoxide

radicals ($^{\bullet}O_2^-$), which can be active in the degradation process. Furthermore, holes remaining in the valence band of NH_2-MIL-101(Cr) can partially react with hydroxyl anions to form hydroxyl radicals.

The following photocatalytic reaction equations may occur during the degradation of RhB over NM@CuS samples:

$$NH_2\text{-MIL-101(Cr)} + h\nu \rightarrow h^+(NH_2\text{-MIL-101(Cr)}) + e^-(NH_2\text{-MIL-101(Cr)}) \quad (1)$$

$$CuS + h\nu \rightarrow h^+(CuS) + e^-(CuS) \quad (2)$$

$$e^-(CuS) \rightarrow e^-(NH_2\text{-MIL-101(Cr)}) \quad (3)$$

$$e^- + O_2\,(\text{adsorbed}) \rightarrow O_2^{\bullet-} \quad (4)$$

$$h^+ + H_2O \rightarrow {\cdot}OH + H^+ \quad (5)$$

$$O_2^{\bullet-} + (h^+/{}^{\bullet}OH) + RhB \rightarrow \rightarrow \rightarrow CO_2 + H_2O \quad (6)$$

For a better evaluation of the photoactivity of the as-prepared samples during degradation, the degradation of organic dyes in the presence of several existing MOFs-based photocatalysts is summarized in Table 3. These data reveal that the 0.15-NM@CuS composite has an excellent photocatalytic performance towards the degradation of organic dye.

Table 3. Comparisons of the photocatalytic efficiency of some reported MOF based photocatalyst with the as-prepared 0.15-NM@CuS.

Photocatalyst	Dye (ppm)	Catalyst (g/L)	Removal efficiency	Irradiation time (min)	Ref.
NH_2-MIL-101(Cr)@CuS	RhB[1] (10)	0.1	94%	80	This work
TiO_2@ Salicylaldehyde@NH_2-MIL-101(Cr)	MB[2] (30)	0.125	90%	90	[101]
$SrZrO_3$-MOF	Ic[3] (30)	0.4	51%	250	[102]
UiO-66(Zr)@Bi_2MoO_6	RhB (10)	0.5	94%	120	[103]
Phosphotungstic Acid@MIL-53(Fe)	RhB (10)	1	98%	120	[104]
NH_2-MIL-25@Ag_3PO_4	RhB (10)	0.5	74%	30	[105]
$BiVO_4$/MIL 125(Ti)	RhB (10)	0.5	92%	180	[106]
N-TiO_2@ MIL-100(Fe)	RhB (5)	1	93.4%	180	[107]
MOF/$CuWO_4$	MB (10)	0.2	92%	150	[108]
CdS@MIL-53(Fe)	RhB (10)	1	90%	120	[109]
AgI/UiO-66(Zr)	RhB (30)	1	98%	60	[110]
Bi_2WO_6/UiO-66(Zr)	RhB (30)	0.5	98%	180	[111]
BiOBr/NH_2-MIL-125(Ti)	RhB (20)	0.2	98%	100	[112]
Ag_2CO_3/UiO-66(Zr)	RhB (30)	0.5	97%	120	[113]

[1] Rhodamine B, [2] Methylene blue, [3] Indigo carmine

4. Conclusion

In summary, a series of the NM@CuS composite photocatalyst samples were fabricated via a conventional solvothermal approach. The photocatalytic elimination of RhB has demonstrated that the sample containing 0.15 g NH_2-MIL-101(Cr) in the precursor suspension exhibits higher photocatalytic ability compared to other samples, which can be attributed to the following factors: effective visible light absorption in the composite samples compared to pure NH_2-MIL-101(Cr);

higher surface area of the composite sample compared to pure CuS; thriving electron-hole transfer between p-type CuS and n-type NH_2-MIL-101(Cr) in the composite structures, as confirmed by electron lifetime calculation, in comparison with pure MOF and CuS; and sulfur enrichment in the NM@CuS samples. The effective electron-hole transfer between p-CuS and n-type NH_2-MIL-101(Cr) could be related to operational interaction between two components in the structure of the composite samples, resulting from the proper potentials of the conduction and valence bands of p-CuS (CB: -0.653, VB: 1.147) to n-NH_2-MIL-101(Cr) (CB: -0.503, VB: 2.097) which forms a direct Z-scheme mechanism between the two components. The proposed mechanism based on electrochemical analysis and trapping of the reactive transient species indicated that superoxide radicals play a leading part in RhB photodegradation. The stability experiments showed the stability of the photocatalyst during the reaction. Finally, the DFT calculations confirm the band structure of the NH_2-MIL-101(Cr)@CuS nanocomposite and its components used in the experiments, showing higher photocatalytic efficiency in the visible region for the nanocomposite compared to the pristine MIL-101(Cr) and CuS. Based on the obtained results from photocatalytic experiments, electrochemical analysis, and stability tests, this work introduces the CuS nanoparticle as an efficient, low cost, and non-toxic co-catalyst for the fabrication of composite photocatalyst based on MOFs.

Supporting Information

The Supporting Information is available free of charge at

FT-IR spectra of the as-prepared samples, The EDX elemental analysis of the as-prepared samples, XPS data of 0.15-NM@CuS sample, XPS spectrum of C1s, O1s, N1s of the 0.15-NM@CuS sample, PXRD patterns, and FTIR spectrum of the 0.15- NM@CuS sample before and

after the photocatalytic reaction, Photoluminescence spectra of the as-prepared samples and the concentration of Cr(III) during the photocatalytic reaction.

AUTHOR INFORMATION

Corresponding Author

***Corresponding author: Elaheh Kowsari, Tel/Fax.: +98(21)64543295, kowsarie@aut.ac.ir, e_kowsari@yahoo.com**

Acknowledgment

We wish to express our gratitude to the Iran National Science Foundation (INSF) (Project no. 96001364) and Research Affairs Division at the Amirkabir University of Technology of Tehran (AUT) (Grant no. 1235/40) for financial support. This work has used computational facilities of the Advanced Research Computing @ Cardiff (ARCCA) Division, Cardiff University, UK.

612 **References**

613 [1] H. Wang, Y. Liu, M. Li, H. Huang, H.M. Xu, R.J. Hong, H. Shen, Multifunctional TiO2
614 nanowires-modified nanoparticles bilayer film for 3D dye-sensitized solar cells,
615 Optoelectron. Adv. Mater. Rapid Commun. 4 (2010) 1166–1169.

616 [2] M. Hasanpour, M. Hatami, Photocatalytic performance of aerogels for organic dyes removal
617 from wastewaters: Review study, J. Mol. Liq. (2020) 113094.
618 doi:10.1016/j.molliq.2020.113094.

619 [3] S.B. Bagherzadeh, M. Kazemeini, N.M. Mahmoodi, A study of the DR23 dye
620 photocatalytic degradation utilizing a magnetic hybrid nanocomposite of MIL-
621 53(Fe)/CoFe2O4: Facile synthesis and kinetic investigations, J. Mol. Liq. 301 (2020)
622 112427. doi:10.1016/j.molliq.2019.112427.

623 [4] A.M. Awad, R. Jalab, A. Benamor, M.S. Nasser, M.M. Ba-Abbad, M. El-Naas, A.W.
624 Mohammad, Adsorption of organic pollutants by nanomaterial-based adsorbents: An
625 overview, J. Mol. Liq. 301 (2020) 112335. doi:10.1016/j.molliq.2019.112335.

626 [5] N.M. Mahmoodi, M. Oveisi, M. Bakhtiari, B. Hayati, A.A. Shekarchi, A. Bagheri, S.
627 Rahimi, Environmentally friendly ultrasound-assisted synthesis of magnetic zeolitic
628 imidazolate framework - Graphene oxide nanocomposites and pollutant removal from
629 water, J. Mol. Liq. 282 (2019) 115–130. doi:10.1016/j.molliq.2019.02.139.

630 [6] M.M. Ba-Abbad, M.S. Takriff, A.A.H. Kadhum, A.B. Mohamad, A. Benamor, A.W.
631 Mohammad, Solar photocatalytic degradation of 2-chlorophenol with ZnO nanoparticles:
632 optimisation with D-optimal design and study of intermediate mechanisms, Environ. Sci.

Pollut. Res. 24 (2017) 2804–2819. doi:10.1007/s11356-016-8033-y.

[7] M.M. Ba-Abbad, M.S. Takriff, A. Benamor, A.W. Mohammad, Size and shape controlled of α-Fe2O3 nanoparticles prepared via sol–gel technique and their photocatalytic activity, J. Sol-Gel Sci. Technol. 81 (2017) 880–893. doi:10.1007/s10971-016-4228-4.

[8] W. Zhang, R.Z. Zhang, Y. Yin, J.M. Yang, Superior selective adsorption of anionic organic dyes by MIL-101 analogs: Regulation of adsorption driving forces by free amino groups in pore channels, J. Mol. Liq. 302 (2020) 112616. doi:10.1016/j.molliq.2020.112616.

[9] S. Liang, D. Zhang, X. Pu, X. Yao, R. Han, J. Yin, X. Ren, A novel Ag2O/g-C3N4 p-n heterojunction photocatalysts with enhanced visible and near-infrared light activity, Sep. Purif. Technol. 210 (2019) 786–797. doi:10.1016/j.seppur.2018.09.008.

[10] Y. Wu, P. Wang, X. Zhu, Q. Zhang, Z. Wang, Y. Liu, G. Zou, Y. Dai, M.-H. Whangbo, B. Huang, Composite of CH 3 NH 3 PbI 3 with Reduced Graphene Oxide as a Highly Efficient and Stable Visible-Light Photocatalyst for Hydrogen Evolution in Aqueous HI Solution, Adv. Mater. 30 (2018) 1704342. doi:10.1002/adma.201704342.

[11] X. Wang, X. Wang, J. Song, Y. Li, Z. Wang, Y. Gao, A highly efficient TiOX (X = N and P) photocatalyst for inactivation of Microcystis aeruginosa under visible light irradiation, Sep. Purif. Technol. 222 (2019) 99–108. doi:10.1016/j.seppur.2019.04.034.

[12] T. Zhang, M. Liu, Y. Meng, B. Huang, X. Pu, X. Shao, A novel method for the synthesis of Ag3VO4/Ag2VO2PO4 heterojunction photocatalysts with improved visible-light photocatalytic properties, Sep. Purif. Technol. 206 (2018) 149–157. doi:10.1016/j.seppur.2018.05.068.

[13] M. Jahanshahi, E. Kowsari, V. Haddadi-Asl, M. Khoobi, B. Bazri, M. Aryafard, J.H. Lee, F.B. Kadumudi, S. Talebian, N. Kamaly, M. Mehrali, A. Dolatshahi-Pirouz, An innovative and eco-friendly modality for synthesis of highly fluorinated graphene by an acidic ionic liquid: Making of an efficacious vehicle for anti-cancer drug delivery, Appl. Surf. Sci. 515 (2020) 146071. doi:10.1016/j.apsusc.2020.146071.

[14] M. Jahanshahi, E. Kowsari, V. Haddadi-Asl, M. Khoobi, J.H. Lee, F.B. Kadumudi, S. Talebian, N. Kamaly, M. Mehrali, Sericin grafted multifunctional curcumin loaded fluorinated graphene oxide nanomedicines with charge switching properties for effective cancer cell targeting, Int. J. Pharm. 572 (2019) 118791. doi:10.1016/j.ijpharm.2019.118791.

[15] R. Liang, F. Jing, L. Shen, N. Qin, L. Wu, MIL-53(Fe) as a highly efficient bifunctional photocatalyst for the simultaneous reduction of Cr(VI) and oxidation of dyes, J. Hazard. Mater. 287 (2015) 364–372. doi:10.1016/j.jhazmat.2015.01.048.

[16] J. Qiu, X.-F. Zhang, X. Zhang, Y. Feng, Y. Li, L. Yang, H. Lu, J. Yao, Constructing Cd0.5Zn0.5S@ZIF-8 nanocomposites through self-assembly strategy to enhance Cr(VI) photocatalytic reduction, J. Hazard. Mater. 349 (2018) 234–241. doi:10.1016/j.jhazmat.2018.02.009.

[17] Q. Gong, Y. Liu, Z. Dang, Core-shell structured Fe3O4@GO@MIL-100(Fe) magnetic nanoparticles as heterogeneous photo-Fenton catalyst for 2,4-dichlorophenol degradation under visible light, J. Hazard. Mater. 371 (2019) 677–686. doi:10.1016/j.jhazmat.2019.03.019.

[18] Y. Zeng, N. Guo, Y. Song, Y. Zhao, H. Li, X. Xu, J. Qiu, H. Yu, Fabrication of Z-scheme

675 magnetic MoS2/CoFe2O4 nanocomposites with highly efficient photocatalytic activity, J.
676 Colloid Interface Sci. 514 (2018) 664–674. doi:10.1016/j.jcis.2017.12.079.

677 [19] S. Li, J. Cui, X. Wu, X. Zhang, Q. Hu, X. Hou, Rapid in situ microwave synthesis of
678 Fe3O4@MIL-100(Fe) for aqueous diclofenac sodium removal through integrated
679 adsorption and photodegradation, J. Hazard. Mater. 373 (2019) 408–416.
680 doi:10.1016/j.jhazmat.2019.03.102.

681 [20] Y. Deng, L. Tang, C. Feng, G. Zeng, Z. Chen, J. Wang, H. Feng, B. Peng, Y. Liu, Y. Zhou,
682 Insight into the dual-channel charge-charrier transfer path for nonmetal plasmonic tungsten
683 oxide based composites with boosted photocatalytic activity under full-spectrum light,
684 Appl. Catal. B Environ. 235 (2018) 225–237. doi:10.1016/j.apcatb.2018.04.075.

685 [21] Y. Deng, C. Feng, L. Tang, Y. Zhou, Z. Chen, H. Feng, J. Wang, J. Yu, Y. Liu, Ultrathin
686 low dimensional heterostructure composites with superior photocatalytic activity: Insight
687 into the multichannel charge transfer mechanism, Chem. Eng. J. 393 (2020) 124718.
688 doi:10.1016/j.cej.2020.124718.

689 [22] Y. Deng, L. Tang, G. Zeng, Z. Zhu, M. Yan, Y. Zhou, J. Wang, Y. Liu, J. Wang, Insight
690 into highly efficient simultaneous photocatalytic removal of Cr(VI) and 2,4-diclorophenol
691 under visible light irradiation by phosphorus doped porous ultrathin g-C3N4 nanosheets
692 from aqueous media: Performance and reaction mechanism, Appl. Catal. B Environ. 203
693 (2017) 343–354. doi:10.1016/j.apcatb.2016.10.046.

694 [23] Y. Deng, Z. Li, R. Tang, K. Ouyang, C. Liao, Y. Fang, C. Ding, L. Yang, L. Su, D. Gong,
695 What will happen when microorganisms “meet” photocatalysts and photocatalysis?,

Environ. Sci. Nano. 7 (2020) 702–723. doi:10.1039/c9en01318k.

[24] H. Heydari, S.E. Moosavifard, S. Elyasi, M. Shahraki, Nanoporous CuS nano-hollow spheres as advanced material for high-performance supercapacitors, Appl. Surf. Sci. 394 (2017) 425–430. doi:10.1016/j.apsusc.2016.10.138.

[25] B. Zeng, X. Chen, C. Chen, X. Ning, W. Deng, Reduced graphene oxides loaded-ZnS/CuS heteronanostructures as high-activity visible-light-driven photocatalysts, J. Alloys Compd. 582 (2014) 774–779. doi:10.1016/j.jallcom.2013.08.121.

[26] X.-S. Hu, Y. Shen, L.-H. Xu, L.-M. Wang, Y.-J. Xing, Preparation of flower-like CuS by solvothermal method and its photodegradation and UV protection, J. Alloys Compd. 674 (2016) 289–294. doi:10.1016/j.jallcom.2016.03.047.

[27] M. Xin, K. Li, H. Wang, Synthesis of CuS thin films by microwave assisted chemical bath deposition, Appl. Surf. Sci. 256 (2009) 1436–1442. doi:10.1016/j.apsusc.2009.08.104.

[28] H. Lee, B.S. Kwak, N.-K. Park, J.-I. Baek, H.-J. Ryu, M. Kang, Assembly of a check-patterned CuSx–TiO2 film with an electron-rich pool and its application for the photoreduction of carbon dioxide to methane, Appl. Surf. Sci. 393 (2017) 385–396. doi:10.1016/j.apsusc.2016.10.026.

[29] J. Wu, B. Liu, Z. Ren, M. Ni, C. Li, Y. Gong, W. Qin, Y. Huang, C.Q. Sun, X. Liu, CuS/RGO hybrid photocatalyst for full solar spectrum photoreduction from UV/Vis to near-infrared light, J. Colloid Interface Sci. 517 (2018) 80–85. doi:10.1016/j.jcis.2017.09.042.

[30] G. Heidari, M. Rabani, B. Ramezanzadeh, Application of CuS–ZnS PN junction for

716 photoelectrochemical water splitting, Int. J. Hydrogen Energy. 42 (2017) 9545–9552.
717 doi:10.1016/j.ijhydene.2017.01.176.

718 [31] X. Wang, L. Li, Z. Fu, F. Cui, Carbon quantum dots decorated CuS nanocomposite for
719 effective degradation of methylene blue and antibacterial performance, J. Mol. Liq. 268
720 (2018) 578–586. doi:10.1016/j.molliq.2018.07.086.

721 [32] M. Saranya, C. Santhosh, R. Ramachandran, P. Kollu, P. Saravanan, M. Vinoba, S.K. Jeong,
722 A.N. Grace, Hydrothermal growth of CuS nanostructures and its photocatalytic properties,
723 Powder Technol. 252 (2014) 25–32. doi:10.1016/j.powtec.2013.10.031.

724 [33] W. Liu, H. Ji, J. Wang, X. Zheng, J. Lai, J. Ji, T. Li, Y. Ma, H. Li, S. Zhao, Z. Jin, Synthesis
725 and Photo-Response of CuS Thin Films by an In Situ Multi-Deposition Process at Room
726 Temperature: A Facile and Eco-Friendly Approach, Nano. 10 (2015) 1550032.
727 doi:10.1142/S1793292015500320.

728 [34] X. Chen, H. Li, Y. Wu, H. Wu, L. Wu, P. Tan, J. Pan, X. Xiong, Facile fabrication of novel
729 porous graphitic carbon nitride/copper sulfide nanocomposites with enhanced visible light
730 driven photocatalytic performance, J. Colloid Interface Sci. 476 (2016) 132–143.
731 doi:10.1016/j.jcis.2016.05.024.

732 [35] N. Karikalan, R. Karthik, S.-M. Chen, C. Karuppiah, A. Elangovan, Sonochemical
733 Synthesis of Sulfur Doped Reduced Graphene Oxide Supported CuS Nanoparticles for the
734 Non-Enzymatic Glucose Sensor Applications, Sci. Rep. 7 (2017) 2494.
735 doi:10.1038/s41598-017-02479-5.

736 [36] X.-S. Hu, Y. Shen, Y.-T. Zhang, J.-J. Nie, Preparation of flower-like CuS/reduced graphene

oxide(RGO) photocatalysts for enhanced photocatalytic activity, J. Phys. Chem. Solids. 103 (2017) 201–208. doi:10.1016/j.jpcs.2016.12.021.

[37] F. Rashidi, E. Lima, H. Rashidi, A. Rashidi, A. Guzmán, Cooperative effect of gold nanoparticles with CUS aluminium from nanoalumina support in the catalysis of an electron transfer reaction, Appl. Catal. A Gen. 417–418 (2012) 129–136. doi:10.1016/j.apcata.2011.12.032.

[38] J. Zhang, Z. Xiong, C. Li, C. Wu, Exploring a thiol-functionalized MOF for elimination of lead and cadmium from aqueous solution, J. Mol. Liq. 221 (2016) 43–50. doi:10.1016/j.molliq.2016.05.054.

[39] Z. Huang, M. Zhao, S. Wang, L. Dai, L. Zhang, C. Wang, Selective recovery of gold ions in aqueous solutions by a novel trithiocyanuric-Zr based MOFs adsorbent, J. Mol. Liq. 298 (2020) 112090. doi:10.1016/j.molliq.2019.112090.

[40] A.M. Ghaedi, M. Panahimehr, A.R.S. Nejad, S.J. Hosseini, A. Vafaei, M.M. Baneshi, Factorial experimental design for the optimization of highly selective adsorption removal of lead and copper ions using metal organic framework MOF-2 (Cd), J. Mol. Liq. 272 (2018) 15–26. doi:10.1016/j.molliq.2018.09.051.

[41] A.J. Sisi, A. Khataee, M. Fathinia, B. Vahid, Ultrasonic-assisted degradation of a triarylmethane dye using combined peroxydisulfate and MOF-2 catalyst: Synergistic effect and role of oxidative species, J. Mol. Liq. 297 (2020) 111838. doi:10.1016/j.molliq.2019.111838.

[42] N.M. Mahmoodi, S. Keshavarzi, M. Oveisi, S. Rahimi, B. Hayati, Metal-organic framework

(ZIF-8)/inorganic nanofiber (Fe2O3) nanocomposite: Green synthesis and photocatalytic degradation using LED irradiation, J. Mol. Liq. 291 (2019) 111333. doi:10.1016/j.molliq.2019.111333.

[43] M.R. Delsouz Khaki, M.S. Shafeeyan, A.A.A. Raman, W.M.A.W. Daud, Evaluating the efficiency of nano-sized Cu doped TiO2/ZnO photocatalyst under visible light irradiation, J. Mol. Liq. 258 (2018) 354–365. doi:10.1016/j.molliq.2017.11.030.

[44] J.-M. Yang, X.-W. Hu, Y.-X. Liu, W. Zhang, Fabrication of a carbon quantum dots-immobilized zirconium-based metal-organic framework composite fluorescence sensor for highly sensitive detection of 4-nitrophenol, Microporous Mesoporous Mater. 274 (2019) 149–154. doi:10.1016/j.micromeso.2018.07.042.

[45] M. Alvaro, E. Carbonell, B. Ferrer, F.X. Llabrés i Xamena, H. Garcia, Semiconductor Behavior of a Metal-Organic Framework (MOF), Chem. - A Eur. J. 13 (2007) 5106–5112. doi:10.1002/chem.200601003.

[46] Y. Pi, X. Li, Q. Xia, J. Wu, Y. Li, J. Xiao, Z. Li, Adsorptive and photocatalytic removal of Persistent Organic Pollutants (POPs) in water by metal-organic frameworks (MOFs), Chem. Eng. J. 337 (2018) 351–371. doi:10.1016/j.cej.2017.12.092.

[47] D.Y. Lee, D. V. Shinde, S.J. Yoon, K.N. Cho, W. Lee, N.K. Shrestha, S.-H. Han, Cu-Based Metal–Organic Frameworks for Photovoltaic Application, J. Phys. Chem. C. 118 (2014) 16328–16334. doi:10.1021/jp4079663.

[48] D.Y. Ahn, D.Y. Lee, C.Y. Shin, H.T. Bui, N.K. Shrestha, L. Giebeler, Y.-Y. Noh, S.-H. Han, Novel Solid-State Solar Cell Based on Hole-Conducting MOF-Sensitizer

Demonstrating Power Conversion Efficiency of 2.1%, ACS Appl. Mater. Interfaces. 9 (2017) 12930–12935. doi:10.1021/acsami.7b03487.

[49] Y. Wang, Y. Zhang, Z. Jiang, G. Jiang, Z. Zhao, Q. Wu, Y. Liu, Q. Xu, A. Duan, C. Xu, Controlled fabrication and enhanced visible-light photocatalytic hydrogen production of Au@CdS/MIL-101 heterostructure, Appl. Catal. B Environ. 185 (2016) 307–314. doi:10.1016/j.apcatb.2015.12.020.

[50] S. Rahim Pouran, A. Bayrami, A.R. Abdul Aziz, W.M.A. Wan Daud, M.S. Shafeeyan, Ultrasound and UV assisted Fenton treatment of recalcitrant wastewaters using transition metal-substituted-magnetite nanoparticles, J. Mol. Liq. 222 (2016) 1076–1084. doi:10.1016/j.molliq.2016.07.120.

[51] M.R. Delsouz Khaki, M.S. Shafeeyan, A.A.A. Raman, W.M.A.W. Daud, Enhanced UV–Visible photocatalytic activity of Cu-doped ZnO/TiO2 nanoparticles, J. Mater. Sci. Mater. Electron. 29 (2018) 5480–5495. doi:10.1007/s10854-017-8515-9.

[52] M. Oveisi, M.A. Asli, N.M. Mahmoodi, MIL-Ti metal-organic frameworks (MOFs) nanomaterials as superior adsorbents: Synthesis and ultrasound-aided dye adsorption from multicomponent wastewater systems, J. Hazard. Mater. 347 (2018) 123–140. doi:10.1016/j.jhazmat.2017.12.057.

[53] S. Abdpour, E. Kowsari, M.R.A. Moghaddam, Synthesis of MIL-100(Fe)@MIL-53(Fe) as a novel hybrid photocatalyst and evaluation photocatalytic and photoelectrochemical performance under visible light irradiation, J. Solid State Chem. 262 (2018) 172–180. doi:10.1016/j.jssc.2018.03.018.

[54] N.M. Mahmoodi, J. Abdi, Nanoporous metal-organic framework (MOF-199): Synthesis, characterization and photocatalytic degradation of Basic Blue 41, Microchem. J. 144 (2019) 436–442. doi:10.1016/j.microc.2018.09.033.

[55] J. Yu, S. Wang, J. Low, W. Xiao, Enhanced photocatalytic performance of direct Z-scheme g-C3N4–TiO2 photocatalysts for the decomposition of formaldehyde in air, Phys. Chem. Chem. Phys. 15 (2013) 16883. doi:10.1039/c3cp53131g.

[56] J. He, Z. Yan, J. Wang, J. Xie, L. Jiang, Y. Shi, F. Yuan, F. Yu, Y. Sun, Significantly enhanced photocatalytic hydrogen evolution under visible light over CdS embedded on metal–organic frameworks, Chem. Commun. 49 (2013) 6761. doi:10.1039/c3cc43218a.

[57] S. Abdpour, E. Kowsari, M.R. Alavi Moghaddam, L. Schmolke, C. Janiak, Mil-100(Fe) nanoparticles supported on urchin like Bi2S3 structure for improving photocatalytic degradation of rhodamine-B dye under visible light irradiation, J. Solid State Chem. 266 (2018) 54–62. doi:10.1016/j.jssc.2018.07.006.

[58] W. Zhan, Q. Kuang, J. Zhou, X. Kong, Z. Xie, L. Zheng, Semiconductor@Metal–Organic Framework Core–Shell Heterostructures: A Case of ZnO@ZIF-8 Nanorods with Selective Photoelectrochemical Response, J. Am. Chem. Soc. 135 (2013) 1926–1933. doi:10.1021/ja311085e.

[59] A. Crake, K.C. Christoforidis, A. Kafizas, S. Zafeiratos, C. Petit, CO 2 capture and photocatalytic reduction using bifunctional TiO 2 /MOF nanocomposites under UV–vis irradiation, Appl. Catal. B Environ. 210 (2017) 131–140. doi:10.1016/j.apcatb.2017.03.039.

[60] Y. Zhang, D. Lan, Y. Wang, H. Cao, H. Jiang, MOF-5 decorated hierarchical ZnO nanorod

821 arrays and its photoluminescence, Phys. E Low-Dimensional Syst. Nanostructures. 43
822 (2011) 1219–1223. doi:10.1016/j.physe.2011.02.004.

823 [61] Y. Cui, L. Nengzi, J. Gou, Y. Huang, B. Li, X. Cheng, Fabrication of dual Z-scheme MIL-
824 53(Fe)/α-Bi2O3/g-C3N4 ternary composite with enhanced visible light photocatalytic
825 performance, Sep. Purif. Technol. 232 (2020) 115959. doi:10.1016/j.seppur.2019.115959.

826 [62] Q. Xu, L. Zhang, J. Yu, S. Wageh, A.A. Al-Ghamdi, M. Jaroniec, Direct Z-scheme
827 photocatalysts: Principles, synthesis, and applications, Mater. Today. 21 (2018) 1042–1063.
828 doi:10.1016/j.mattod.2018.04.008.

829 [63] A. Khutia, H.U. Rammelberg, T. Schmidt, S. Henninger, C. Janiak, Water Sorption Cycle
830 Measurements on Functionalized MIL-101Cr for Heat Transformation Application, Chem.
831 Mater. 25 (2013) 790–798. doi:10.1021/cm304055k.

832 [64] F. Li, J. Wu, Q. Qin, Z. Li, X. Huang, Controllable synthesis, optical and photocatalytic
833 properties of CuS nanomaterials with hierarchical structures, Powder Technol. 198 (2010)
834 267–274. doi:10.1016/j.powtec.2009.11.018.

835 [65] B. Bazri, E. Kowsari, N. Seifvand, N. Naseri, RGO-α-Fe2O3/β-FeOOH ternary
836 heterostructure with urchin-like morphology for efficient oxygen evolution reaction, J.
837 Electroanal. Chem. 843 (2019) 1–11. doi:10.1016/j.jelechem.2019.04.069.

838 [66] P. Hohenberg, W. Kohn, Inhomogeneous Electron Gas, Phys. Rev. 136 (1964) B864–B871.
839 doi:10.1103/PhysRev.136.B864.

840 [67] W. Kohn, L.J. Sham, Self-Consistent Equations Including Exchange and Correlation

841 Effects, Phys. Rev. 140 (1965) A1133–A1138. doi:10.1103/PhysRev.140.A1133.

842 [68] G. Kresse, J. Furthmüller, Efficiency of ab-initio total energy calculations for metals and
843 semiconductors using a plane-wave basis set, Comput. Mater. Sci. 6 (1996) 15–50.
844 doi:10.1016/0927-0256(96)00008-0.

845 [69] G. Kresse, J. Furthmüller, Efficient iterative schemes for ab initio total-energy calculations
846 using a plane-wave basis set, Phys. Rev. B. 54 (1996) 11169–11186.
847 doi:10.1103/PhysRevB.54.11169.

848 [70] J.P. Perdew, K. Burke, M. Ernzerhof, Generalized Gradient Approximation Made Simple,
849 Phys. Rev. Lett. 77 (1996) 3865–3868. doi:10.1103/PhysRevLett.77.3865.

850 [71] P.E. Blöchl, Projector augmented-wave method, Phys. Rev. B. 50 (1994) 17953–17979.
851 doi:10.1103/PhysRevB.50.17953.

852 [72] S.S. Tafreshi, A. Roldan, N.H. de Leeuw, Density Functional Theory Study of the
853 Adsorption of Hydrazine on the Perfect and Defective Copper (100), (110), and (111)
854 Surfaces, J. Phys. Chem. C. 118 (2014) 26103–26114. doi:10.1021/jp5078664.

855 [73] S. Grimme, S. Ehrlich, L. Goerigk, Effect of the damping function in dispersion corrected
856 density functional theory, J. Comput. Chem. 32 (2011) 1456–1465. doi:10.1002/jcc.21759.

857 [74] J. Paier, R. Hirschl, M. Marsman, G. Kresse, The Perdew–Burke–Ernzerhof exchange-
858 correlation functional applied to the G2-1 test set using a plane-wave basis set, J. Chem.
859 Phys. 122 (2005) 234102. doi:10.1063/1.1926272.

860 [75] X. Wu, I. Choudhuri, D.G. Truhlar, Computational Studies of Photocatalysis with Metal–

861 Organic Frameworks, ENERGY Environ. Mater. 2 (2019) 251–263.
862 doi:10.1002/eem2.12051.

863 [76] Á. Morales-García, J. He, A.L. Soares, H.A. Duarte, Surfaces and morphologies of covellite
864 (CuS) nanoparticles by means of ab initio atomistic thermodynamics, CrystEngComm. 19
865 (2017) 3078–3084. doi:10.1039/C7CE00203C.

866 [77] H.J. Monkhorst, J.D. Pack, Special points for Brillouin-zone integrations, Phys. Rev. B. 13
867 (1976) 5188–5192. doi:10.1103/PhysRevB.13.5188.

868 [78] X. Huang, J. Lu, W. Wang, X. Wei, J. Ding, Experimental and computational investigation
869 of CO2 capture on amine grafted metal-organic framework NH2-MIL-101, Appl. Surf. Sci.
870 371 (2016) 307–313. doi:10.1016/j.apsusc.2016.02.154.

871 [79] D. Jiang, L.L. Keenan, A.D. Burrows, K.J. Edler, Synthesis and post-synthetic modification
872 of MIL-101(Cr)-NH2via a tandem diazotisation process, Chem. Commun. 48 (2012) 12053.
873 doi:10.1039/c2cc36344e.

874 [80] M. Venkata-Haritha, C.V.V.M. Gopi, L. Young-Seok, H.-J. Kim, Controlled growth of a
875 nanoplatelet-structured copper sulfide thin film as a highly efficient counter electrode for
876 quantum dot-sensitized solar cells, RSC Adv. 6 (2016) 45809–45818.
877 doi:10.1039/C6RA08375G.

878 [81] H.-J. Kim, L. Myung-Sik, C.V.V.M. Gopi, M. Venkata-Haritha, S.S. Rao, S.-K. Kim, Cost-
879 effective and morphology controllable PVP based highly efficient CuS counter electrodes
880 for high-efficiency quantum dot-sensitized solar cells, Dalt. Trans. 44 (2015) 11340–11351.
881 doi:10.1039/C5DT01412C.

[82] X.-L. Yu, C.-B. Cao, H.-S. Zhu, Q.-S. Li, C.-L. Liu, Q.-H. Gong, Nanometer-Sized Copper Sulfide Hollow Spheres with Strong Optical-Limiting Properties, Adv. Funct. Mater. 17 (2007) 1397–1401. doi:10.1002/adfm.200600245.

[83] S.H. Chaki, J.P. Tailor, M.P. Deshpande, Covellite CuS – Single crystal growth by chemical vapour transport (CVT) technique and characterization, Mater. Sci. Semicond. Process. 27 (2014) 577–585. doi:10.1016/j.mssp.2014.07.038.

[84] M.C. Biesinger, B.P. Payne, A.P. Grosvenor, L.W.M. Lau, A.R. Gerson, R.S.C. Smart, Resolving surface chemical states in XPS analysis of first row transition metals, oxides and hydroxides: Cr, Mn, Fe, Co and Ni, Appl. Surf. Sci. 257 (2011) 2717–2730. doi:10.1016/j.apsusc.2010.10.051.

[85] M.C. Biesinger, B.R. Hart, R. Polack, B.A. Kobe, R.S.C. Smart, Analysis of mineral surface chemistry in flotation separation using imaging XPS, Miner. Eng. 20 (2007) 152–162. doi:10.1016/j.mineng.2006.08.006.

[86] C. Song, X. Wang, J. Zhang, X. Chen, C. Li, Enhanced performance of direct Z-scheme CuS-WO3 system towards photocatalytic decomposition of organic pollutants under visible light, Appl. Surf. Sci. 425 (2017) 788–795. doi:10.1016/j.apsusc.2017.07.082.

[87] M. Wen, K. Mori, T. Kamegawa, H. Yamashita, Amine-functionalized MIL-101(Cr) with imbedded platinum nanoparticles as a durable photocatalyst for hydrogen production from water, Chem. Commun. 50 (2014) 11645–11648. doi:10.1039/C4CC02994A.

[88] P. Zhang, L. Gao, Copper sulfide flakes and nanodisks, J. Mater. Chem. 13 (2003) 2007. doi:10.1039/b305584a.

[89] C. Ratanatawanate, A. Bui, K. Vu, K.J. Balkus, Low-Temperature Synthesis of Copper(II) Sulfide Quantum Dot Decorated TiO 2 Nanotubes and Their Photocatalytic Properties, J. Phys. Chem. C. 115 (2011) 6175–6180. doi:10.1021/jp109716q.

[90] J.P. Park, J.H. Heo, S.H. Im, S.-W. Kim, Highly efficient solid-state mesoscopic PbS with embedded CuS quantum dot-sensitized solar cells, J. Mater. Chem. A. 4 (2016) 785–790. doi:10.1039/C5TA08668J.

[91] Z. Chen, H. Jiang, W. Jin, C. Shi, Enhanced photocatalytic performance over Bi4Ti3O12 nanosheets with controllable size and exposed {0 0 1} facets for Rhodamine B degradation, Appl. Catal. B Environ. 180 (2016) 698–706. doi:10.1016/j.apcatb.2015.07.022.

[92] V. Augugliaro, C. Baiocchi, A. Bianco Prevot, E. García-López, V. Loddo, S. Malato, G. Marcí, L. Palmisano, M. Pazzi, E. Pramauro, Azo-dyes photocatalytic degradation in aqueous suspension of TiO2 under solar irradiation, Chemosphere. 49 (2002) 1223–1230. doi:10.1016/S0045-6535(02)00489-7.

[93] M. Dorraj, M. Alizadeh, N.A. Sairi, W.J. Basirun, B.T. Goh, P.M. Woi, Y. Alias, Enhanced visible light photocatalytic activity of copper-doped titanium oxide–zinc oxide heterojunction for methyl orange degradation, Appl. Surf. Sci. 414 (2017) 251–261. doi:10.1016/j.apsusc.2017.04.045.

[94] W. Zhao, Y. Liu, Z. Wei, S. Yang, H. He, C. Sun, Fabrication of a novel p–n heterojunction photocatalyst n-BiVO4@p-MoS2 with core–shell structure and its excellent visible-light photocatalytic reduction and oxidation activities, Appl. Catal. B Environ. 185 (2016) 242–252. doi:10.1016/j.apcatb.2015.12.023.

924 [95] M. Yan, Y. Hua, F. Zhu, W. Gu, J. Jiang, H. Shen, W. Shi, Fabrication of nitrogen doped
925 graphene quantum dots-BiOI/MnNb2O6 p-n junction photocatalysts with enhanced visible
926 light efficiency in photocatalytic degradation of antibiotics, Appl. Catal. B Environ. 202
927 (2017) 518–527. doi:10.1016/j.apcatb.2016.09.039.

928 [96] C. Venkata Thulasi-Varma, S.S. Rao, C.S.S.P. Kumar, C.V.V.M. Gopi, I.K. Durga, S.K.
929 Kim, D. Punnoose, H.J. Kim, Enhanced photovoltaic performance and time varied
930 controllable growth of a CuS nanoplatelet structured thin film and its application as an
931 efficient counter electrode for quantum dot-sensitized solar cells via a cost-effective
932 chemical bath deposition, Dalt. Trans. 44 (2015) 19330–19343. doi:10.1039/c5dt02182k.

933 [97] P.-Y. Kuang, Y.-Z. Su, G.-F. Chen, Z. Luo, S.-Y. Xing, N. Li, Z.-Q. Liu, g-C3N4 decorated
934 ZnO nanorod arrays for enhanced photoelectrocatalytic performance, Appl. Surf. Sci. 358
935 (2015) 296–303. doi:10.1016/j.apsusc.2015.08.066.

936 [98] L. Zhang, M. Jaroniec, Toward designing semiconductor-semiconductor heterojunctions for
937 photocatalytic applications, Appl. Surf. Sci. 430 (2018) 2–17.
938 doi:10.1016/j.apsusc.2017.07.192.

939 [99] J. Wang, Y. Yu, L. Zhang, Highly efficient photocatalytic removal of sodium
940 pentachlorophenate with Bi3O4Br under visible light, Appl. Catal. B Environ. 136–137
941 (2013) 112–121. doi:10.1016/j.apcatb.2013.02.009.

942 [100] H.T. Evans, J.A. Konnert, Crystal structure refinement of covellite, Am. Mineral. 61 (1976)
943 996–1000.

944 [101] X. Li, Y. Pi, Q. Xia, Z. Li, J. Xiao, TiO2 encapsulated in Salicylaldehyde-NH2-MIL-

945 101(Cr) for enhanced visible light-driven photodegradation of MB, Appl. Catal. B Environ.
946 191 (2016) 192–201. doi:10.1016/j.apcatb.2016.03.034.

947 [102] L.A. Alfonso-Herrera, A.M. Huerta-Flores, L.M. Torres-Martínez, J.M. Rivera-Villanueva,
948 D.J. Ramírez-Herrera, Hybrid SrZrO3-MOF heterostructure: surface assembly and
949 photocatalytic performance for hydrogen evolution and degradation of indigo carmine dye,
950 J. Mater. Sci. Mater. Electron. 29 (2018) 10395–10410. doi:10.1007/s10854-018-9096-y.

951 [103] J. Ding, Z. Yang, C. He, X. Tong, Y. Li, X. Niu, H. Zhang, UiO-66(Zr) coupled with Bi 2
952 MoO 6 as photocatalyst for visible-light promoted dye degradation, J. Colloid Interface Sci.
953 497 (2017) 126–133. doi:10.1016/j.jcis.2017.02.060.

954 [104] L. Narayanasamy, T. Murugesan, Degradation of Alizarin Yellow R using UV/H 2 O 2
955 advanced oxidation process, Environ. Prog. Sustain. Energy. 33 (2014) 482–489.
956 doi:10.1002/ep.11816.

957 [105] R.M. Abdelhameed, D.M. Tobaldi, M. Karmaoui, Engineering highly effective and stable
958 nanocomposite photocatalyst based on NH2-MIL-125 encirclement with Ag3PO4
959 nanoparticles, J. Photochem. Photobiol. A Chem. 351 (2018) 50–58.
960 doi:10.1016/j.jphotochem.2017.10.011.

961 [106] Z. Yang, J. Ding, J. Feng, C. He, Y. Li, X. Tong, X. Niu, H. Zhang, Preparation of BiVO 4
962 /MIL-125(Ti) composite with enhanced visible-light photocatalytic activity for dye
963 degradation, Appl. Organomet. Chem. 32 (2018) e4285. doi:10.1002/aoc.4285.

964 [107] J. Huang, H. Song, C. Chen, Y. Yang, N. Xu, X. Ji, C. Li, J.-A. You, Facile synthesis of N-
965 doped TiO2 nanoparticles caged in MIL-100(Fe) for photocatalytic degradation of organic

966 dyes under visible light irradiation, J. Environ. Chem. Eng. 5 (2017) 2579–2585.
967 doi:10.1016/j.jece.2017.05.012.

968 [108] H. Ramezanalizadeh, F. Manteghi, Synthesis of a novel MOF/CuWO4 heterostructure for
969 efficient photocatalytic degradation and removal of water pollutants, J. Clean. Prod. 172
970 (2018) 2655–2666. doi:10.1016/j.jclepro.2017.11.145.

971 [109] L. Hu, G. Deng, W. Lu, S. Pang, X. Hu, Deposition of CdS nanoparticles on MIL-53(Fe)
972 metal-organic framework with enhanced photocatalytic degradation of RhB under visible
973 light irradiation, Appl. Surf. Sci. 410 (2017) 401–413. doi:10.1016/j.apsusc.2017.03.140.

974 [110] Z. Sha, J. Sun, H.S.O. Chan, S. Jaenicke, J. Wu, Enhanced Photocatalytic Activity of the
975 AgI/UiO-66(Zr) Composite for Rhodamine B Degradation under Visible-Light Irradiation,
976 Chempluschem. 80 (2015) 1321–1328. doi:10.1002/cplu.201402430.

977 [111] Z. Sha, J. Sun, H.S. On Chan, S. Jaenicke, J. Wu, Bismuth tungstate incorporated zirconium
978 metal–organic framework composite with enhanced visible-light photocatalytic
979 performance, RSC Adv. 4 (2014) 64977–64984. doi:10.1039/C4RA13000F.

980 [112] S.-R. Zhu, P.-F. Liu, M.-K. Wu, W.-N. Zhao, G.-C. Li, K. Tao, F.-Y. Yi, L. Han, Enhanced
981 photocatalytic performance of BiOBr/NH 2 -MIL-125(Ti) composite for dye degradation
982 under visible light, Dalt. Trans. 45 (2016) 17521–17529. doi:10.1039/C6DT02912D.

983 [113] Z. Sha, H.S.O. Chan, J. Wu, Ag2CO3/UiO-66(Zr) composite with enhanced visible-light
984 promoted photocatalytic activity for dye degradation, J. Hazard. Mater. 299 (2015) 132–
985 140. doi:10.1016/j.jhazmat.2015.06.016.

986